

Possibility of multi-step electroweak phase transition in the two Higgs doublet models

Mayumi Aoki^{1, a}, Takatoshi Komatsu^{1, b} and Hiroto Shibuya^{1, c}

¹*Institute for Theoretical Physics, Kanazawa University, Kanazawa 920-1192, Japan*

We discuss whether a multi-step electroweak phase transition (EWPT) occurs in two Higgs doublet models (2HDMs). The EWPT is related to interesting phenomena such as baryogenesis and a gravitational wave from it. We examine parameter regions in CP-conserving 2HDMs and find certain areas where the multi-step EWPTs occur. The parameter search shows the multi-step EWPT prefers the scalar potential with the approximate Z_2 symmetry and a mass hierarchy between the neutral CP-odd and CP-even extra scalar bosons $m_A < m_H$. By contrast, the multi-step EWPT whose first step is strongly first order favors a mass hierarchy $m_A > m_H$. In addition, we compute the Higgs trilinear coupling in the parameter region where the multi-step EWPTs occur, which can be observed at future colliders. We also discuss a multi-peaked gravitational wave from a multi-step EWPT.

I. INTRODUCTION

Although the standard model (SM) of particle physics is verified through various experiments, the asymmetry of baryon number in the universe is still one of the big problems. The observable of a baryon to radiation number ratio is $\eta_B \equiv n_B/n_\gamma = (6.12 \pm 0.04) \times 10^{-10}$ [1]. To explain this asymmetry, the theory must satisfy Sakharov's three conditions [2]. The conditions are violation of baryon numbers, violation of C and CP symmetries, and departure from thermal equilibrium. To generate baryon asymmetry at the electroweak (EW) scale via EW baryogenesis (EWBG) [3], the EW phase transition (EWPT) is needed to be strongly first order. However, the lattice simulations show that the mass of Higgs boson must be less than about 70 GeV to make the EWPT first order in the SM [4, 5] and the observed Higgs boson with the mass of 125 GeV [6–9] indicates that the EWPT in the SM is cross over [10]. Furthermore, sufficient baryon asymmetry cannot be produced via the Cabibbo-Kobayashi-Maskawa phase, so that the EWBG cannot be achieved successfully in the SM [11–13]. The sufficient baryon asymmetry can be generated via the EWBG scenario by extending the scalar sector of the SM. One of the simplest extensions is the two Higgs doublet model (2HDM), where a $SU(2)$ scalar doublet is added to the SM¹. Since the 2HDM has new CP-violating sources in the scalar potential, it has a possibility of achieving the EWBG. However, the model has difficulty producing sufficient baryon number because the electric dipole moment (EDM) measurements constrain the sources strictly [21–23]².

One could come up with the idea to solve the above difficulty in the 2HDMs by considering a multi-step EWPT [25]. The sufficient baryon number is produced at the first step PT if it is the strongly first order and enough CP violation exists, while the baryon number cannot be washed out at the subsequent PT(s) if EW sphaleron processes are suppressed enough. Consequently, sufficient baryon number is preserved at the EW vacuum even if it is a CP-conserving vacuum. The reason why we consider baryon asymmetry produced at the first step is that the first order PT

^a mayumi.aoki@staff.kanazawa-u.ac.jp

^b t_komatsu@hep.s.kanazawa-u.ac.jp

^c h_shibuya@hep.s.kanazawa-u.ac.jp

¹ As studies for the strong 1-step PTs in the CP-conserving 2HDMs, see *e.g.* Refs. [14–18]. For the non-perturbative analyses, see Refs. [19, 20].

² In the aligned 2HDM, there are possibilities to evade the EDM constraints through cancellations among contributions to the EDMs even when CP-violating phases are unsuppressed [24].

at the subsequent step occurs between $SU(2)$ broken phases. Therefore the sphaleron processes are suppressed in both phases and the sufficient asymmetry would not be produced [26, 27]³. Another interesting phenomenon derived from the multi-step PT is the multi-peaked gravitational wave (GW). Since the first order PT yields a GW spectrum [28, 29], the superposed GW can have multiple peaks if the first order PT occurs multiple times, which could be observed by the future space-based interferometers such as the approved Laser Interferometer Space Antenna (LISA) [30–32]. The previous researches concerning multi-step PTs are in the singlet extensions [33–47], inert 2HDMs [25, 26, 48–50], 2HDMs [16, 27, 51], triplet extensions [52–55], and the other models [56–70].

In this paper, we study the multi-step EWPTs in the CP-conserving 2HDMs. Because of the absence of the new CP-violating source, the EWBG does not work and we would not discuss it. The study for the CP-violating case remains as future work. The main purpose of this paper is to reveal features of the multi-step PTs. By performing parameter searches, we find certain parameter spaces where the multi-step PT occurs. Furthermore to examine the possibility of verification of the multi-step PT at collider experiments, we compute the deviation of the Higgs trilinear coupling from that in the SM. It is known that the deviation can be large in the 2HDMs [71, 72] (see also Ref. [73, 74] for recent work), and it would be observed more precisely in future colliders like High-Luminosity Large Hadron Collider (HL-LHC) [75] and International Linear Collider (ILC) [76]. We find that the deviation has a tendency to be large in certain regions when the multi-step PTs occur. In addition, we calculate a two-peaked GW spectrum yielded by a 2-step PT, which can be observed by using LISA, Big Bang Observer (BBO) [77], and Ultimate Deci-Hertz Interferometer Gravitational Wave Observatory (U-DECIGO) [78].

The outline of this paper is as follows: In section II we introduce the generic characteristics of the 2HDMs. Section III is dedicated to give the thermal effective potential. Theoretical constraints considered in our numerical analyses are briefly introduced in Section IV. In section V we show the results of the parameter search for the multi-step PT. Moreover, in section VI, we discuss the predictions for the Higgs trilinear couplings as the collider signatures and for the multi-peaked GW as the cosmological signature for the multi-step PT. Our conclusions are given in section VII.

II. TWO HIGGS DOUBLET MODEL

The tree-level scalar potential of the CP-conserving 2HDMs with a softly broken Z_2 symmetry is written as

$$V(\Phi_1, \Phi_2) = m_1^2 \Phi_1^\dagger \Phi_1 + m_2^2 \Phi_2^\dagger \Phi_2 - m_3^2 (\Phi_1^\dagger \Phi_2 + \Phi_2^\dagger \Phi_1) + \frac{\lambda_1}{2} (\Phi_1^\dagger \Phi_1)^2 + \frac{\lambda_2}{2} (\Phi_2^\dagger \Phi_2)^2 + \lambda_3 (\Phi_1^\dagger \Phi_1) (\Phi_2^\dagger \Phi_2) + \lambda_4 (\Phi_1^\dagger \Phi_2) (\Phi_2^\dagger \Phi_1) + \frac{\lambda_5}{2} \left[(\Phi_1^\dagger \Phi_2)^2 + (\Phi_2^\dagger \Phi_1)^2 \right], \quad (1)$$

where Φ_i ($i = 1, 2$) are the $SU(2)$ scalar doublets

$$\Phi_i = \begin{pmatrix} w_i^+ \\ \frac{v_i + h_i + iz_i}{\sqrt{2}} \end{pmatrix}. \quad (2)$$

We here assume that only the neutral CP-even scalar fields have the vacuum expectation values (VEVs) v_i , which are real and positive, and satisfy $v \equiv \sqrt{v_1^2 + v_2^2} = 246$ GeV. The third term with m_3^2 on the right-hand side in Eq. (1) breaks the Z_2 symmetry in the potential softly. The

³ Ref. [26] shows that sufficient baryon asymmetry is difficult to be generated at the subsequent PT in the inert 2HDM. In Ref. [27], it is also mentioned that the second step PT would not generate sufficient asymmetry in the 2HDMs.

coefficients are taken to be real, although m_3^2 and λ_5 are complex parameters in general. Regarding only the neutral CP-even fields ϕ_i , the Φ_i become

$$\Phi_i = \begin{pmatrix} 0 \\ \frac{\phi_i}{\sqrt{2}} \end{pmatrix}. \quad (3)$$

Consequently, the tree-level scalar potential (1) with the doublets (3) is

$$V_0(\phi_1, \phi_2) = \frac{m_1^2}{2}\phi_1^2 + \frac{m_2^2}{2}\phi_2^2 - m_3^2\phi_1\phi_2 + \frac{\lambda_1}{8}\phi_1^4 + \frac{\lambda_2}{8}\phi_2^4 + \frac{1}{4}(\lambda_3 + \lambda_4 + \lambda_5)(\phi_1\phi_2)^2. \quad (4)$$

The minimum value of $V_0(\phi_1, \phi_2)$ given by $\phi_i = v_i$. From the minimum conditions, $\partial V_0/\partial\phi_i|_{\phi_i=v_i} = 0$, we obtain

$$m_1^2 = m_3^2 \frac{v_2}{v_1} - \frac{\lambda_1}{2}v_1^2 - \frac{1}{2}(\lambda_3 + \lambda_4 + \lambda_5)v_2^2, \quad (5)$$

$$m_2^2 = m_3^2 \frac{v_1}{v_2} - \frac{\lambda_2}{2}v_2^2 - \frac{1}{2}(\lambda_3 + \lambda_4 + \lambda_5)v_1^2. \quad (6)$$

To calculate the effective potential, we introduce the field-dependent masses because we need the masses of all fields at each of the coordinates (ϕ_1, ϕ_2) , which contribute to the potential at the loop-level. The field-dependent mass matrices of the charged and the neutral CP-odd scalar fields in the gauge basis are respectively given by

$$\begin{aligned} \mathcal{M}_{w^\pm}^2 &= \frac{1}{2} \begin{pmatrix} 2m_1^2 + \lambda_1\phi_1^2 + \lambda_3\phi_2^2 & -2m_3^2 + (\lambda_4 + \lambda_5)\phi_1\phi_2 \\ -2m_3^2 + (\lambda_4 + \lambda_5)\phi_1\phi_2 & 2m_2^2 + \lambda_2\phi_2^2 + \lambda_3\phi_1^2 \end{pmatrix}, \\ \mathcal{M}_z^2 &= \frac{1}{2} \begin{pmatrix} 2m_1^2 + \lambda_1\phi_1^2 + (\lambda_3 + \lambda_4 - \lambda_5)\phi_2^2 & -2m_3^2 + 2\lambda_5\phi_1\phi_2 \\ -2m_3^2 + 2\lambda_5\phi_1\phi_2 & 2m_2^2 + \lambda_2\phi_2^2 + (\lambda_3 + \lambda_4 - \lambda_5)\phi_1^2 \end{pmatrix}. \end{aligned} \quad (7)$$

By taking $\phi_i = v_i$ and diagonalizing these matrices, the physical masses of the charged scalar field H^\pm and the neutral CP-odd scalar field A are respectively obtained as

$$m_{H^\pm}^2 = \frac{m_3^2}{\sin\beta\cos\beta} - \frac{1}{2}(\lambda_4 + \lambda_5)v^2, \quad (8a)$$

$$m_A^2 = \frac{m_3^2}{\sin\beta\cos\beta} - \lambda_5v^2, \quad (8b)$$

where we have introduced the angle β as $\tan\beta \equiv v_2/v_1$. On the other hand, the physical squared-masses of the neutral CP-even scalar fields H and h can be derived by diagonalizing the mass matrix

$$\mathcal{M}_h^2 = \frac{1}{2} \begin{pmatrix} 2m_1^2 + 3\lambda_1\phi_1^2 + (\lambda_3 + \lambda_4 + \lambda_5)\phi_2^2 & -2m_3^2 + 2(\lambda_3 + \lambda_4 + \lambda_5)\phi_1\phi_2 \\ -2m_3^2 + 2(\lambda_3 + \lambda_4 + \lambda_5)\phi_1\phi_2 & 2m_2^2 + 3\lambda_2\phi_2^2 + (\lambda_3 + \lambda_4 + \lambda_5)\phi_1^2 \end{pmatrix}, \quad (9)$$

with $\phi_i = v_i$ as

$$\begin{pmatrix} m_H^2 & 0 \\ 0 & m_h^2 \end{pmatrix} = R(-\alpha)\mathcal{M}_h^2R(\alpha), \quad \text{with } R(\alpha) \equiv \begin{pmatrix} \cos\alpha & -\sin\alpha \\ \sin\alpha & \cos\alpha \end{pmatrix}. \quad (10)$$

Here, the squared masses m_H^2 and m_h^2 are obtained by

$$\begin{aligned} m_H^2 &= \frac{1}{2} \left[A + C + \sqrt{(A - C)^2 + 4B^2} \right], \\ m_h^2 &= \frac{1}{2} \left[A + C - \sqrt{(A - C)^2 + 4B^2} \right], \end{aligned} \quad (11)$$

	Φ_1	Φ_2	u_R	d_R	l_R	Q_L, L_L
Type-I	+	-	-	-	-	+
Type-II	+	-	-	+	+	+
Type-X	+	-	-	-	+	+
Type-Y	+	-	-	+	-	+

TABLE I. Four types in the 2HDMs distinguished by Z_2 charges for each of the fermions.

with

$$A = m_3^2 \tan \beta + \lambda_1 v^2 \cos^2 \beta, \quad (12)$$

$$B = -m_3^2 + (\lambda_3 + \lambda_4 + \lambda_5) v^2 \sin \beta \cos \beta, \quad (13)$$

$$C = \frac{m_3^2}{\tan \beta} + \lambda_2 v^2 \sin^2 \beta. \quad (14)$$

Throughout this paper we take h as the SM-like Higgs boson with $m_h = 125$ GeV.

The field-dependent masses of the W boson, the Z boson, and the photon can be written as

$$\begin{aligned} m_W &= \frac{1}{2} g \sqrt{\phi_1^2 + \phi_2^2}, \\ m_Z &= \frac{1}{2} \sqrt{g^2 + g'^2} \sqrt{\phi_1^2 + \phi_2^2}, \\ m_\gamma &= 0, \end{aligned} \quad (15)$$

where g and g' are the gauge couplings of $SU(2)_L$ and $U(1)_Y$ gauge symmetry, respectively. The physical masses of the gauge bosons are derived by taking $\phi_i = v_i$.

The most general Yukawa term is

$$\mathcal{L}_{\text{Yukawa}} = -\bar{Q}_L Y_u \tilde{\Phi}_u u_R - \bar{Q}_L Y_d \Phi_d d_R - \bar{L}_L Y_l \Phi_l l_R + \text{h.c.}, \quad (16)$$

where Q_L and L_L are $SU(2)_L$ doublets of quarks and leptons, respectively, Y_f ($f = u, d, l$) are the Yukawa matrices of the fermions, and each of Φ_f is either Φ_1 or Φ_2 . Since the 2HDMs have the two $SU(2)$ scalar doublets, we assume one of the doublets couples each of the fermions to avoid the tree-level flavor changing neutral current. One of ways to accomplish this is assuming 2HDMs have a Z_2 symmetry. In this case, there are 4 types in the 2HDMs distinguished by the Z_2 charges for each of the fermions as in the Tab. I [79–81]. In the Type-I 2HDM, all quarks and charged leptons obtain their masses from the VEV of Φ_2 . In the Type-II 2HDM, the VEV of Φ_2 gives the masses of the up-type quarks, while that of Φ_1 provides those of the down-type quarks and the charged leptons. In the Type-X 2HDM, the charged leptons and quarks obtain their masses from the VEV of Φ_1 and Φ_2 , respectively. In the Type-Y 2HDM, the masses of the down-type quarks are generated by the VEV of Φ_1 , while those of the up-type quarks and the charged leptons are obtained by that of Φ_2 . The field-dependent masses of fermions can be described as

$$m_f = \frac{1}{\sqrt{2}} y_f \phi_i, \quad (17)$$

where which value assigned to i depends on the types of Yukawa interactions. The physical masses of the fermions are obtained by taking $\phi_i = v_i$.

III. THE EFFECTIVE POTENTIAL AT FINITE TEMPERATURE

A. The one-loop corrected effective potential

An EWPT is caused by the temperature change of the effective scalar potential. To study the PT, we consider the thermal effective potential. The one-loop corrected effective potential at the finite temperature V^β is

$$V^\beta = V_0 + V_{\text{CW}} + V_{\text{CT}} + \bar{V}_1^\beta, \quad (18)$$

where V_0 , V_{CW} , V_{CT} , and \bar{V}_1^β are the tree-level potential (4), the one-loop level potential at zero temperature (the Coleman-Weinberg potential), the counterterm potential, and the one-loop level potential at the finite temperature, respectively.

The Coleman-Weinberg potential in the $\overline{\text{MS}}$ scheme is written by [82]

$$V_{\text{CW}}(\phi_1, \phi_2) = \pm \frac{1}{64\pi^2} \sum_k n_k m_k^4(\phi_1, \phi_2) \left[\log \frac{m_k^2(\phi_1, \phi_2)}{\mu^2} - c_k \right], \quad (19)$$

where k indicates scalar and gauge bosons and fermions, and n_k , m_k , and μ are the degrees of freedom of each fields, the field-dependent masses of each fields, and the renormalization scale which we set $\mu = 246$ GeV, respectively. The upper (lower) sign corresponds to the bosonic (fermionic) contribution. The corresponding degrees of freedom are $n_k = 2, 1, 1, 1, 6, 3, 2, 12, 12$, and 4 for $k = H^\pm, H, h, A, W, Z, \gamma, t, b$, and τ , respectively. We only consider the fermions which have the non-negligible contributions. The constant c_k are equal to 1/2 for transverse gauge bosons and 3/2 for the other particles in the $\overline{\text{MS}}$ scheme.

The V_{CW} changes the coordinate of the global minimum of the potential from that of V_0 . We introduce the counterterm potential V_{CT} for fixing the coordinate, the masses and the mixing angles of the scalar fields to be equal to the tree-level ones. Thus, we impose the following five conditions to determine V_{CT} :

$$\left. \frac{\partial V_{\text{CT}}(\phi_1, \phi_2)}{\partial \phi_i} \right|_{(\phi_1, \phi_2)=(v_1, v_2)} = - \left. \frac{\partial V_{\text{CW}}(\phi_1, \phi_2)}{\partial \phi_i} \right|_{(\phi_1, \phi_2)=(v_1, v_2)}, \quad (20a)$$

$$\left. \frac{\partial^2 V_{\text{CT}}(\phi_1, \phi_2)}{\partial \phi_i \partial \phi_j} \right|_{(\phi_1, \phi_2)=(v_1, v_2)} = - \left. \frac{\partial^2 V_{\text{CW}}(\phi_1, \phi_2)}{\partial \phi_i \partial \phi_j} \right|_{(\phi_1, \phi_2)=(v_1, v_2)} \quad (i, j = 1, 2). \quad (20b)$$

Following Ref. [16], we set V_{CT} with five parameters δm_1^2 , δm_2^2 , $\delta \lambda_1$, $\delta \lambda_2$, and $\delta \lambda_{345}$,

$$V_{\text{CT}} = \delta m_1^2 \phi_1^2 + \delta m_2^2 \phi_2^2 + \delta \lambda_1 \phi_1^4 + \delta \lambda_2 \phi_2^4 + \delta \lambda_{345} \phi_1^2 \phi_2^2. \quad (21)$$

Hence, the conditions (20) give

$$\begin{aligned} \delta m_1^2 &= -\frac{3}{4v_1} V_1 + \frac{1}{4} V_{11} + \frac{1}{4} \frac{v_2}{v_1} V_{12}, \\ \delta m_2^2 &= -\frac{3}{4v_2} V_2 + \frac{1}{4} V_{22} + \frac{1}{4} \frac{v_1}{v_2} V_{12}, \\ \delta \lambda_1 &= \frac{1}{8v_1^3} (V_1 - v_1 V_{11}), \\ \delta \lambda_2 &= \frac{1}{8v_2^3} (V_2 - v_2 V_{22}), \\ \delta \lambda_{345} &= -\frac{V_{12}}{4v_1 v_2}, \end{aligned} \quad (22)$$

where $V_i \equiv \partial V_{\text{CW}}/\partial\phi_i|_{(v_1, v_2)}$ and $V_{ij} \equiv \partial^2 V_{\text{CW}}/(\partial\phi_i\partial\phi_j)|_{(v_1, v_2)}$. We calculate δm_1^2 , δm_2^2 , $\delta\lambda_1$, $\delta\lambda_2$, and $\delta\lambda_{345}$ numerically and substitute them for V_{CT} . However, there are infrared divergences in the second derivatives of V_{CW} , which are proportional to $\log m_{\text{NG}}^2$ where m_{NG} indicate the masses of Nambu-Goldstone (NG) bosons. To avoid these divergences, we use the approximation which is shown in Ref. [83]. In this approximation, m_{NG} are approximated as the mass of the SM-like Higgs boson, i.e. $m_{\text{NG}} \rightarrow m_h$. This approximation is justified because the divergences are only logarithmic, hence the changes of the masses of the NG bosons do not make large differences.

The one-loop thermal contributions to the potential can be written as [84]

$$\bar{V}_1^\beta(\phi_1, \phi_2) = \pm \frac{T^4}{2\pi^2} \sum_k \int dx x^2 \ln \left[1 \mp \exp \left(-\sqrt{x^2 + \frac{m_k^2(\phi_1, \phi_2)}{T^2}} \right) \right], \quad (23)$$

where T represents the temperature and the upper (lower) sign indicates the bosonic (fermionic) contribution. We calculate the integral in Eq. (23) numerically. The squared-masses of the scalar bosons in Eq. (23) can become negative for certain sets of the coordinate (ϕ_1, ϕ_2) and T ⁴. In that case, we adopt a method that is discarding the imaginary part of the thermal potential, which is related to the instability of the field configuration [85], and taking only the real part (e.g. Ref. [15]).

B. Resummation

Although V^β contains the corrections to the one-loop level, the contributions of higher loop diagrams get larger as the temperature rises. The dominant diagrams at the high temperature are called daisy diagrams [84]. We perform resummation which is the method for taking into account the corrections from the diagrams [86, 87]. Although there are two methods for the resummation, we apply the Parwani method [86]⁵. The resummation is achieved by appending the corrections from the scalar and gauge boson polarization tensors in the infrared limit $\Pi_B(T)$ to the masses of bosons m_B^2

$$m_B^2(\phi_1, \phi_2) \rightarrow m_B^2(\phi_1, \phi_2) + \Pi_B(T), \quad (24)$$

and inserting these corrected masses to \bar{V}_1^β in Eq. (23) [89]. The index B represents the species of bosons.

In the 2HDMs, we carry out the resummation concretely as the following. The resummation for scalar fields are performed by adding the contributions of the two-point functions to the mass parameters m_1 and m_2 in the mass matrices Eqs. (7) and (9) [90]

$$m_i^2 \rightarrow m_i^2 + c_i T^2, \quad (25)$$

where c_i are the coefficients of correction terms and determined by $\Pi_B(T)$ which depends on the types of Yukawa interactions. In the Type-I 2HDM, they can be written by [16]

⁴ We comment on the region for the negative scalar squared-masses in Appendix A. The negative quadratic parameters sometimes yield the negative squared-masses at finite temperature, so we would discuss the region involved with Fig. 4.

⁵ There is another method of resummation, called the Arnold-Epinosa (AE) method [87]. The method takes into account only bosonic Matsubara zero-modes which are involved in infrared divergences and adds cubic terms to the potential. The procedure uses the high-temperature expansion when dividing the thermal contributions into those of the zero and non-zero modes. Hence, it would be unsuccessful in regions where the high-temperature expansion is not valid. In our calculation of the multi-step EWPT, we need to consider the PT near the EW vacuum in some cases (cf. Fig. 5), where the high-temperature expansion is broken because the condition of the expansion, $m_B/T < 1$, would not be satisfied. Therefore, the AE method is not suitable for the computation of the multi-step EWPT. In contrast to the AE method, the Parwani method can take the non-relativistic limit smoothly even if theories include heavy particles [83, 88] since the method does not contain the high-temperature expansion.

$$c_1 = \frac{1}{8}g^2 + \frac{1}{16}(g^2 + g'^2) + \frac{1}{4}\lambda_1 + \frac{1}{6}\lambda_3 + \frac{1}{12}\lambda_4, \quad (26a)$$

$$c_2 = \frac{1}{8}g^2 + \frac{1}{16}(g^2 + g'^2) + \frac{1}{4}\lambda_2 + \frac{1}{6}\lambda_3 + \frac{1}{12}\lambda_4 + \frac{1}{4}y_t^2 + \frac{1}{4}y_b^2 + \frac{1}{12}y_\tau^2. \quad (26b)$$

For the other Yukawa types, one can obtain the coefficients by apportioning the Yukawa coupling terms in Eq. (26) to c_1 and c_2 according to Tab. I. And then, we append the correction terms to the non-diagonalized scalar matrices $\mathcal{M}_{w^\pm}^2$, \mathcal{M}_z^2 , and \mathcal{M}_h^2 in Eqs. (7) and (9) as

$$\mathcal{M}_{w^\pm}^2 + \begin{pmatrix} c_1 & 0 \\ 0 & c_2 \end{pmatrix} T^2, \quad \mathcal{M}_z^2 + \begin{pmatrix} c_1 & 0 \\ 0 & c_2 \end{pmatrix} T^2, \quad \mathcal{M}_h^2 + \begin{pmatrix} c_1 & 0 \\ 0 & c_2 \end{pmatrix} T^2, \quad (27)$$

and obtain the corrected scalar masses by diagonalizing them.

For the gauge fields, one can carry out the resummation by appending the contributions to only the longitudinal component of the mass matrices. Following Ref. [90], the corrected masses of the longitudinal W boson can be written by

$$M_{W_L}^2 = \frac{g^2}{4}(\phi_1^2 + \phi_2^2) + 2g^2 T^2. \quad (28)$$

The corrected mass matrix of the longitudinally polarized Z boson and photon in the gauge basis is

$$\frac{1}{4}(\phi_1^2 + \phi_2^2) \begin{pmatrix} g^2 & -gg' \\ -gg' & g'^2 \end{pmatrix} + \begin{pmatrix} 2g^2 T^2 & 0 \\ 0 & 2g'^2 T^2 \end{pmatrix}. \quad (29)$$

By diagonalizing it, the corrected masses of the Z boson and the photon are obtained as

$$\begin{aligned} M_{Z_L}^2 &= \frac{1}{8}(g^2 + g'^2)(\phi_1^2 + \phi_2^2 + 8T^2) + \Delta, \\ M_{\gamma_L}^2 &= \frac{1}{8}(g^2 + g'^2)(\phi_1^2 + \phi_2^2 + 8T^2) - \Delta, \end{aligned} \quad (30)$$

with

$$\Delta = \sqrt{\left[\frac{1}{8}(g^2 + g'^2)(\phi_1^2 + \phi_2^2 + 8T^2) \right]^2 - g^2 g'^2 T^2 (\phi_1^2 + \phi_2^2 + 4T^2)}. \quad (31)$$

IV. THEORETICAL CONSTRAINTS AND EW-VACUUM STABILITY

For the theoretical constraints on the model, we consider constraints from the boundedness from below (BFB) of V_0 , which is described as [91–94]

$$\lambda_1 > 0, \quad \lambda_2 > 0, \quad -\sqrt{\lambda_1 \lambda_2} < \lambda_3, \quad -\sqrt{\lambda_1 + \lambda_2} < \lambda_3 + \lambda_4 - \lambda_5, \quad (32)$$

the perturbativity,

$$|\lambda_n| < 4\pi \quad (n = 1, 2, \dots, 5), \quad (33)$$

and the tree-level unitarity [95, 96].

Furthermore the absolute tree-level stability of the EW vacuum is required [97, 98], where the negative m_3^2 is disfavored. In following analyses, we confirm numerically that the EW vacuum is the global minimum in the region for $|\phi_i| \leq 10$ TeV, and remove the cases where $\sqrt{\phi_1^2 + \phi_2^2} = 246$ GeV is not satisfied at the global minimum.

	m_A [GeV]	m_H [GeV]	$\tan\beta$	$\cos(\beta - \alpha)$	m_3 [GeV]
Type-I ($m_A = m_{H^\pm}$)	180–1000(/10)	130–1000(/10)	2–10(/0.5)	−0.25–0.25(/0.05)	0–100
Type-I ($m_H = m_{H^\pm}$)	130–1000(/10)	180–1000(/10)	2–10(/0.5)	−0.25–0.25(/0.05)	0–100
Type-X ($m_A = m_{H^\pm}$)	180–1000(/10)	130–1000(/10)	2–10(/0.5)	0	0–100
Type-X ($m_H = m_{H^\pm}$)	130–1000(/10)	180–1000(/10)	2–10(/0.5)	0	0–100

TABLE II. Parameter regions studied in the Type-I and Type-X 2HDMs with m_A or $m_H = m_{H^\pm}$. We perform analyses in every 10 GeV in the masses of the neutral scalar bosons, 0.5 in $\tan\beta$, 0.05 in $\cos(\beta - \alpha)$ (though we set $\cos(\beta - \alpha) = 0$ in the Type-X 2HDMs), and 5 GeV in m_3 .

V. NUMERICAL RESULTS

In this section, we discuss the parameter space where the multi-step PT occurs. To study the PT, CosmoTransitions [99] is used in the analyses. We also study the region where the strongly first order PT occurs in the multi-step PT. The strength of the PT ξ is defined by

$$\xi \equiv \frac{v_c}{T_c}, \quad (34)$$

where T_c is the critical temperature, at which minima degenerate between two phases, and v_c is the critical value of $\sqrt{\phi_1^2 + \phi_2^2}$ at T_c . As the criterion for a strong PT, we consider $\xi \geq 1$, where the sphaleron processes are suppressed enough in the $SU(2)$ broken phase. We especially focus on the cases that the first step PTs of the 2-step PTs are strongly first order⁶, which we name “the strong 2-step PTs”⁷. In this case, the sphaleron rate is suppressed in the broken phase, and it is expected that v_c and T_c at the subsequent step PTs are respectively larger and smaller than the previous PT. Therefore, the inequality $\xi \geq 1$ is kept and the sphaleron rate is also suppressed at the subsequent step PTs⁸.

In the following analysis, instead of the eight parameters (m_1^2 , m_2^2 , m_3^2 , λ_{1-5}) in V_0 , we take the following set as the input parameters:

$$m_{H^\pm}, m_A, m_H, \tan\beta, \cos(\beta - \alpha), m_3, m_h, v. \quad (35)$$

Here $m_h = 125$ GeV and $v = 246$ GeV. In order to put restrictions on the range of the other input parameters, we consider the experimental constraints from the EW precision data, the $B \rightarrow X_s \gamma$ decays, the $H^\pm \rightarrow \tau\nu$ decays, and the coupling measurements of the Higgs boson. The EW precision data can be satisfied by assuming the mass degeneracy between the charged scalar boson and at least one of the extra neutral scalar bosons, $m_{H^\pm} \simeq m_A$ or m_H , which makes the custodial symmetry recovered and hence the ρ parameter $\rho \simeq 1$ like in the SM [100]. For m_{H^\pm} , the range $m_{H^\pm} < 590$ GeV is excluded from $B \rightarrow X_s \gamma$ decays in the Type-II and -Y 2HDMs [101], while $m_{H^\pm} \leq 170$ GeV is excluded from $H^\pm \rightarrow \tau\nu$ decays in the Type-X 2HDM [102]. The constraints from the coupling measurements of the Higgs boson [103] show that *e.g.*, $|\cos(\beta - \alpha)| > 0.25$ (0.3) is excluded at $\tan\beta = 2$ (10) in the Type-I 2HDM, and $|\cos(\beta - \alpha)| > 0.15$ (0.05) is excluded at $\tan\beta = 2$ (10) in the Type-X 2HDM. In the Type-II and -Y 2HDMs, the constraints are stricter than those in the Type-I and -X 2HDMs.

In our analyses, based on the above constraints, we take the range for the input parameters in the Type-I and -X 2HDMs as shown in Tab. II. Imposing the mass degeneracy $m_\Phi = m_{H^\pm}$

⁶ We take into account the first order, the second order, and the cross-over PTs as the first step PTs.

⁷ The strong 3-step PTs (i.e. the 3-step PTs where the first step PT is strongly first order) are found in the Type-I 2HDMs, where they occur in the region that the strong 2-step PTs happen in. However the number of points for such PTs is much smaller than that for the strong 2-step PTs, hence we do not discuss the results. Note that we cannot find such PTs in the Type-X 2HDMs.

⁸ If baryon number is generated at the first step PT (although our model cannot generate baryon number since the CP is conserved), it remains unwashed-out.

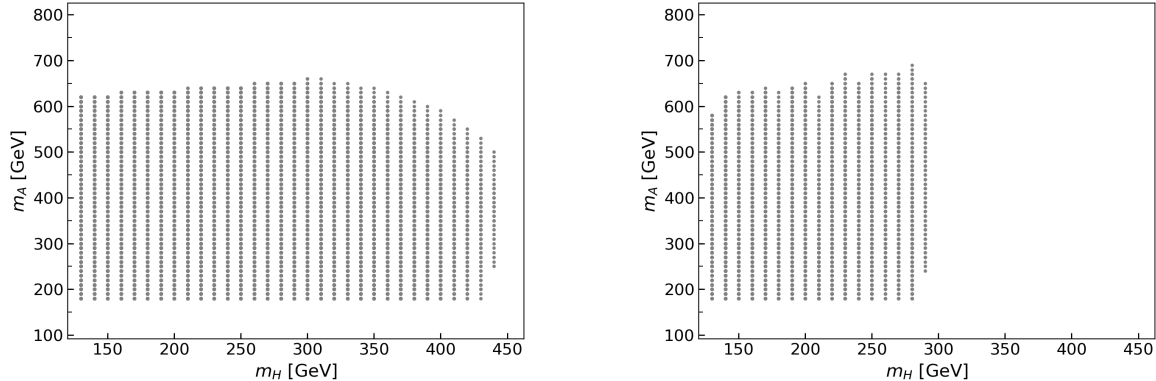


FIG. 1. Parameter regions in the m_A vs. m_H plane allowed by the theoretical constraints (the BFB, the perturbativity, and the tree-level unitarity) in the Type-I 2HDM with $m_A = m_{H^\pm}$. The left and right panel show the regions in the cases of $\tan\beta = 2$ and 7, respectively. The other input parameters follow Tab. II.

($\Phi = H$ or A), the ranges for m_A and m_H are taken as 180 GeV–1 TeV for m_Φ and 130 GeV–1 TeV for the other extra neutral scalar boson. For the mixing angles, we take $\tan\beta = 2 - 10$, and $|\cos(\beta - \alpha)| \leq 0.25$ in the Type-I 2HDM, while the *alignment limit*, $\cos(\beta - \alpha) = 0$, in the Type-X 2HDM. In the analyses we focus on the relatively small value for m_3 as $0 \leq m_3 \leq 100$ GeV, since the strong 2-step PTs which we are interested in prefer to occur for the smaller m_3 and do not occur for $m_3 \simeq 100$ GeV (cf. Fig. 6). As depicted in Tab. II, we take every 10 GeV in m_A and m_H , 0.5 in $\tan\beta$, 0.05 in $\cos(\beta - \alpha)$ (though we set $\cos(\beta - \alpha) = 0$ in the Type-X 2HDMs), and 5 GeV in m_3 .

In the Type-II and -Y 2HDMs, we take the same ranges for the input parameters with those in the Type-X 2HDM, but $m_\Phi = m_{H^\pm} \geq 590$ GeV by the constraint from $B \rightarrow X_s \gamma$. In these cases, we have found that the stability of the EW vacuum is not realized because the contributions of the heavy extra scalar fields lift up the potential significantly at the EW vacuum (see Eq. (19)) and the origin $(\phi_1, \phi_2) = (0, 0)$ becomes the global minimum. Hence we discuss only Type-I and -X 2HDMs hereafter.

A. Type-I

1. Type-I ($m_A = m_{H^\pm}$)

In this subsection, we show the results in the Type-I 2HDM with $m_A = m_{H^\pm}$. Fig. 1 represents the allowed parameter region by the theoretical constraints (the BFB, the perturbativity, and the tree-level unitarity) in the m_A vs. m_H plane at $\tan\beta = 2$ (left) and 7 (right). It shows in the case of $\tan\beta = 7$ the upper limit on m_H is lower than that in the case of $\tan\beta = 2$, as $m_H \lesssim 290$ (440) GeV for $\tan\beta = 7$ (2).

The left panels of Fig. 2 exhibit the parameter points where the 1-step and multi-step PTs (left) occur in the m_A vs. m_H (top), m_A vs. $\tan\beta$ (middle), and m_A vs. $\cos(\beta - \alpha)$ (bottom) planes. The yellow, blue, and purple points show the results for the 1-step, 2-step, and 3 or more step PTs, respectively⁹. Here in addition to the theoretical constraints considered in Fig. 1, the constraint for the stability of the EW vacuum is further imposed. Compared the top left panel in Fig. 2 with Fig. 1, we can see that the region with the larger m_A (and m_H) is excluded by

⁹ The “3 or more step PTs” includes the 4-step PTs. The numbers of points for 3-step and 4-step PTs account for about 1% and 0.1% of the number of all points in this case, respectively.

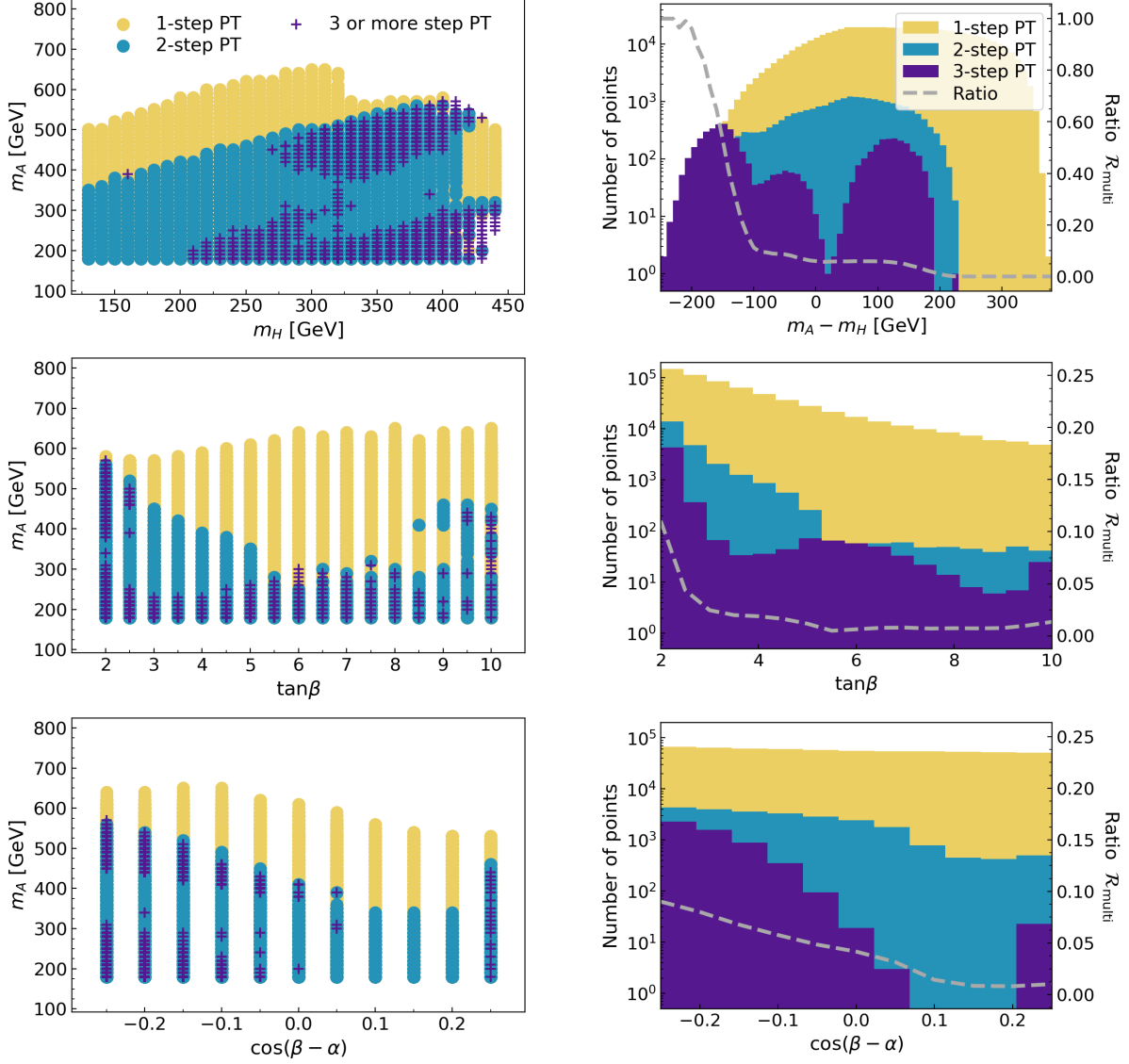


FIG. 2. Left: Parameter points where the 1-step and multi-step PTs occur in the m_A vs. m_H (top), m_A vs. $\tan\beta$ (middle), and m_A vs. $\cos(\beta - \alpha)$ (bottom) planes in the Type-I 2HDM with $m_A = m_{H^\pm}$. The yellow, blue, and purple points show the results for the 1-step, 2-step, and 3 or more step PTs, respectively. Right: Number of points where the 1-step and multi-step PTs occur as a function of $m_A - m_H$ (top), $\tan\beta$ (middle) and $\cos(\beta - \alpha)$ (bottom). The 1-step, 2-step, and 3 or more step PTs are colored by yellow, blue, and purple, respectively. The grey dashed lines in the panels represent $\mathcal{R}_{\text{multi}}$, which are the ratios of the number of points for the multi-step PTs to that for all PTs.

the constraint. In the left panels of Fig. 2, the range of m_A where the multi-step PTs occur gets larger, as m_H increases, and $\tan\beta$ and $\cos(\beta - \alpha)$ (except for $\tan\beta \simeq 10$ and $\cos(\beta - \alpha) \simeq 0.25$) respectively decreases. In the top left panel of Fig. 2, the parameter region of the multi-step PTs overlaps with that of the 1-step PTs, but for the region where $m_H \simeq 420$ GeV with $m_A \simeq 550$ GeV or 200–300 GeV, the 3 or more step PTs occur mostly. The right panels in Fig. 2 represent the number of points for the 1-step (yellow), 2-step (blue), 3 or more step PTs (purple), respectively, as a function of $m_A - m_H$ (top), $\tan\beta$ (middle) and $\cos(\beta - \alpha)$ (bottom). The ratios $\mathcal{R}_{\text{multi}}$ in the panels, plotted as grey dashed lines, are the ratios of the number of points for the multi-step PTs

to that for all PTs,

$$\mathcal{R}_{\text{multi}} = \frac{\# \text{ of points for the multi-step PTs}}{\# \text{ of points for all PTs}}. \quad (36)$$

We see that, in the top right panel of Fig. 2, the multi-step PTs favor $m_A - m_H < 0$, and the ratio $\mathcal{R}_{\text{multi}} \simeq 1$ is obtained at $m_A - m_H \simeq -210$ GeV. Hence, when $\mathcal{R}_{\text{multi}}$ becomes around 1, $m_H \gtrsim 390$ GeV and m_A is around 200 GeV. Moreover, the middle and bottom right panels of Fig. 2 show that $\mathcal{R}_{\text{multi}}$ becomes larger for the smaller $\tan\beta$ and $\cos(\beta - \alpha)$, and reaches about 10% at $\tan\beta = 2$ and $\cos(\beta - \alpha) = -0.25$, respectively. For $\tan\beta \simeq 10$ and $\cos(\beta - \alpha) \simeq 0.25$, we can see that $\mathcal{R}_{\text{multi}}$ are only a few %, respectively, although the allowed ranges of m_A for the multi-step PTs are wide in the middle and bottom left panels in Fig. 2.

As expected from Fig. 1, the regions with $m_H \simeq 420$ GeV are realized for $\tan\beta \simeq 2$ in this analysis. In such a low $\tan\beta$ case, the $B \rightarrow \mu^+\mu^-$ process gives the constraint on m_{H^\pm} as *e.g.*, $m_{H^\pm} > 340$ (125) GeV at $\tan\beta \simeq 2$ (3) at 95%CL in the Type-I and -X 2HDMs [101]. Therefore the region where the 3 or more step PTs occur mostly with $m_H \simeq 420$ GeV and $m_A (= m_{H^\pm}) \simeq 200\text{--}300$ GeV is excluded by the constraint from $B \rightarrow \mu^+\mu^-$. We have found that even when the constraint is taken into account in this analysis, the multi-step PTs favor the mass hierarchy $m_A < m_H$ and *e.g.*, $\mathcal{R}_{\text{multi}} \simeq 100\%$ (10%) is obtained at $m_A - m_H \simeq -150$ (-80) GeV. Moreover, we should note that if $m_A - m_H < -m_Z$, the region would be constrained by the extra Higgs boson search $H \rightarrow AZ$ at the LHC [104–106]. It is generally more severe for the low $\tan\beta$ and the $\cos(\beta - \alpha)$ closer to zero [107, 108]. We leave the detailed analyses including the constraints from such extra Higgs boson searches for future work.

The left panels of Fig. 3 show the parameter points where the 2-step and strong 2-step PTs occur in the m_A vs. m_H (top), m_A vs. $\tan\beta$ (middle), and m_A vs. $\cos(\beta - \alpha)$ (bottom) planes as well as Fig. 2. The blue and dark-blue points present the parameter points where the 2-step and strong 2-step PTs occur, respectively. From the top left panel of Fig. 3, we can see that the strong 2-step PTs happen in the region where $m_A \gtrsim 300$ GeV and $m_H \lesssim 350$ GeV, and the mass hierarchy $m_A > m_H$ exists. Additionally, in the middle and bottom left panels of Fig. 3, the range of m_A where the strong 2-step PTs happen increases as $\tan\beta$ and $\cos(\beta - \alpha)$ becomes smaller, respectively. Here the strong 2-step PTs occur only in $\tan\beta \lesssim 5$. The right panels in Fig. 3 exhibit the number of points for the 2-step (blue) and strong 2-step PTs (dark-blue), respectively, as a function of $m_A - m_H$ (top), $\tan\beta$ (middle) and $\cos(\beta - \alpha)$ (bottom). The ratios \mathcal{R}_{st2} in the right panels are the ratios of the number of points for the strong 2-step PTs to that for the 2-step PTs,

$$\mathcal{R}_{\text{st2}} = \frac{\# \text{ of points for the strong 2-step PTs}}{\# \text{ of points for the 2-step PTs}}, \quad (37)$$

which are shown by green dashed lines. It is notable that in the top right panel of Fig. 3 the strong 2-step PTs favor $m_A - m_H > 0$ and \mathcal{R}_{st2} becomes $\mathcal{R}_{\text{st2}} = 100\%$ at $m_A - m_H \simeq 210$ GeV. Moreover, the strong 2-step PTs are likely to occur at the small $\tan\beta$ and $\cos(\beta - \alpha)$, respectively, as shown in the middle and bottom right panels of Fig. 3. The parameter regions of the strong 2-step PTs do not receive the constraint from $B \rightarrow \mu^+\mu^-$, while some of them with $m_A - m_H > m_Z$ could be constrained from the $A \rightarrow HZ$ decay at the LHC [107, 108].

The multi-step PTs tend to occur for the smaller $\tan\beta$ and $\cos(\beta - \alpha)$. Next, we investigate the correlations between these parameters and m_2^2 that is an important parameter to determine the path of PT. As we will see later in Fig. 5, the VEVs after the first step in the multi-step PTs have a tendency to be located mainly along the ϕ_2 axis. Therefore we expect that m_2^2 should be negative and have large enough magnitude to make the multi-step PTs occur because such m_2^2

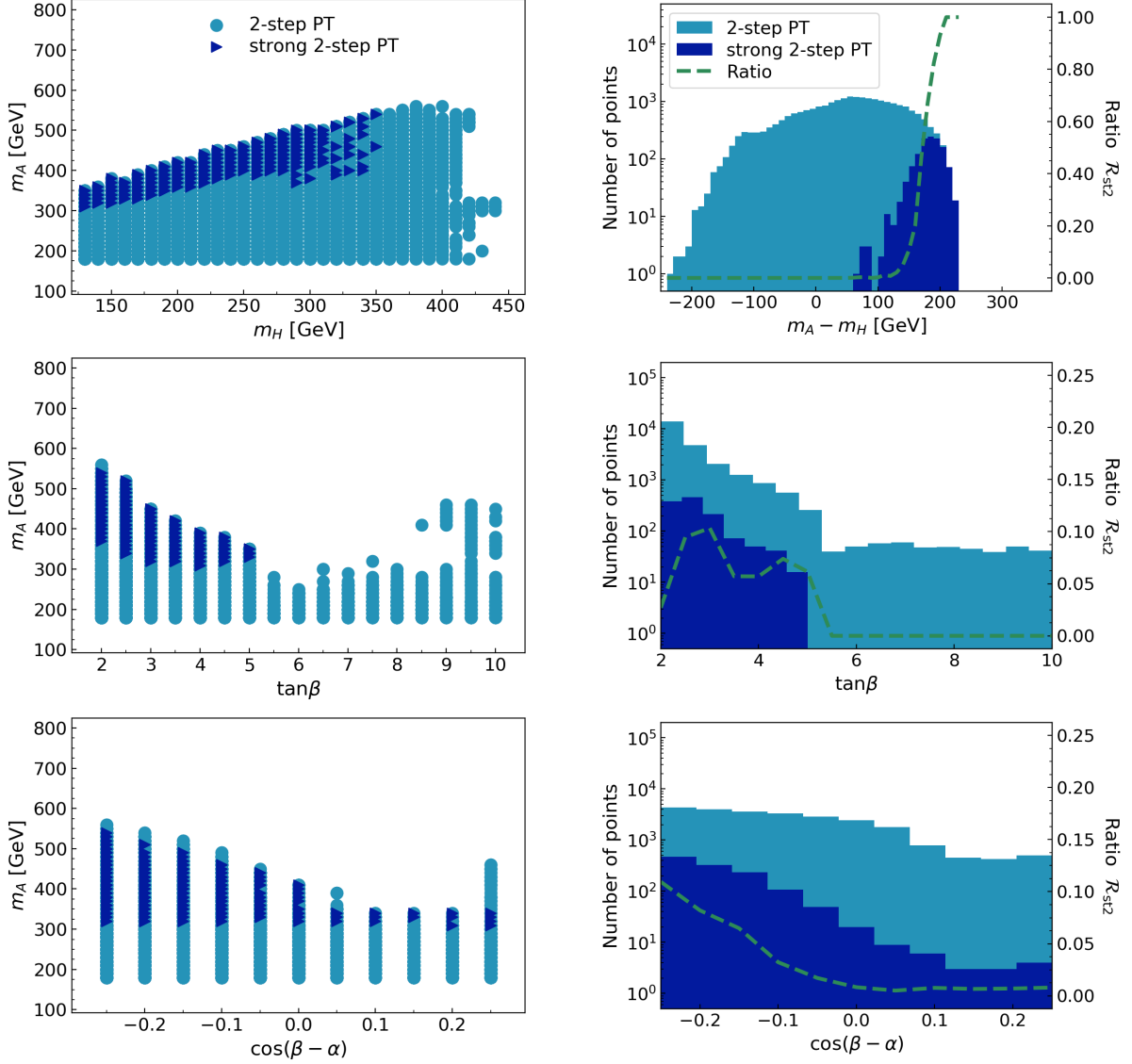


FIG. 3. Left: Parameter points where the 2-step and strong 2-step PTs occur in the m_A vs. m_H (top), m_A vs. $\tan\beta$ (middle), and m_A vs. $\cos(\beta - \alpha)$ (bottom) planes in the Type-I 2HDM with $m_A = m_{H^\pm}$. The blue and dark-blue points present the parameter points where the 2-step and strong 2-step PTs occur, respectively. Right: Number of points where the 2-step and strong 2-step PTs occur as a function of $m_A - m_H$ (top), $\tan\beta$ (middle) and $\cos(\beta - \alpha)$ (bottom). The 2-step and strong 2-step PTs are colored by blue and dark-blue, respectively. The green dashed lines in the panels represent $\mathcal{R}_{\text{st}2}$, which are the ratios of the number of points for the strong 2-step PTs to that for 2-step PTs.

makes the potential decrease in the direction of the ϕ_2 axis. From Eq. (6), m_2^2 can be written as

$$m_2^2 = \frac{1}{\tan\beta} \left[m_3^2 - \frac{1}{2}(m_H^2 - m_h^2) \cos\alpha \sin\alpha \right] - \frac{1}{2}(m_h^2 \cos^2\alpha + m_H^2 \sin^2\alpha). \quad (38)$$

In Fig. 4, the regions where the 1-step, 2-step, and 3 or more step PTs occur are shown in the m_2^2 vs. $\tan\beta$ (left) and m_2^2 vs. $\cos(\beta - \alpha)$ (right) plane, respectively. As can be expected, the multi-step PTs occur for the smaller m_2^2 as $m_2^2 \lesssim -0.5 \times 10^4 \text{ GeV}^2$. The minimum value of m_2^2 decreases as $\tan\beta$ and $\cos(\beta - \alpha)$ are smaller, respectively. These features can be understood from Eq. (38). The leading term on the right-hand side of Eq. (38) is the last one, $-\frac{1}{2}m_H^2 \sin^2\alpha$, in our explored

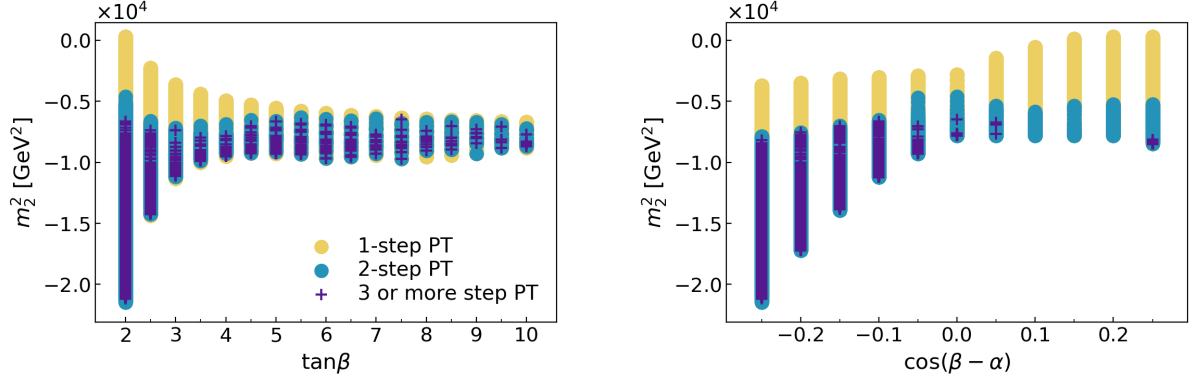


FIG. 4. Parameter points where the 1-step, 2-step, and 3 or more step PTs occur in the m_2^2 vs. $\tan\beta$ (left) and m_2^2 vs. $\cos(\beta - \alpha)$ (right) planes in the Type-I 2HDM with $m_A = m_{H^\pm}$.

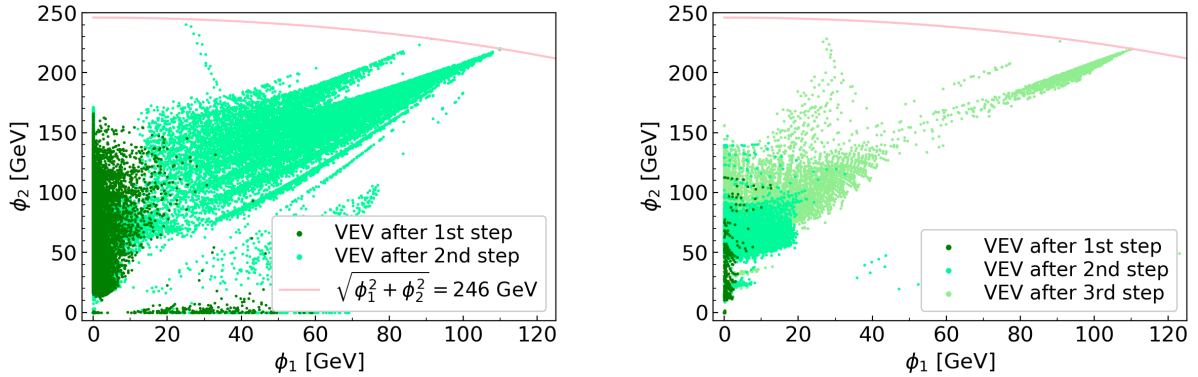


FIG. 5. VEVs after each step of the 2-step (left) and 3-step (right) PTs in the Type-I 2HDM with $m_A = m_{H^\pm}$. The dark-green, green, and light-green points represent the VEVs after the first, the second, and the third step PTs, respectively. The pink line represents the place where $\sqrt{\phi_1^2 + \phi_2^2} = 246$ GeV, that the EW vacuum lies on.

parameter region. Hence, as $m_H |\sin\alpha|$ increases, the negative m_2^2 with the large magnitude can be obtained. As shown in Fig. 1, the larger m_H is allowed for the smaller $\tan\beta$. On the other hand, $|\sin\alpha|$ increases as $\cos(\beta - \alpha)$ gets smaller in our parameter space. Thus, the minimum value of m_2^2 decreases as $\tan\beta$ and $\cos(\beta - \alpha)$ get smaller, respectively. Meanwhile, at $\cos(\beta - \alpha) \simeq 0.2$, $\sin\alpha$ is possible to be zero. In this case, the second and last terms in Eq. (38) vanish and the value of m_H does not affect m_2^2 . However, in the region where $\cos(\beta - \alpha) \simeq 0.25$ and $\tan\beta \simeq 10$, $|\sin\alpha|$ can be large to some extent and the contribution of the last term in Eq. (38) recovers, which leads to the negative m_2^2 with the slightly large magnitude. This case is presented in Fig. 4.

As described above, when m_2^2 is negative with the large magnitude, the first step in the multi-step PT tends to occur along the ϕ_2 axis. In order to see more clearly, we show in Fig. 5 the VEVs after each step of the 2-step (left) and 3-step (right) PTs in the ϕ_2 vs. ϕ_1 plane. The dark-green points indicate the VEVs after the first step PTs and the green points show the ones after the second step PTs. In the right panel of Fig. 5, the light-green points indicate the VEVs after the third step PTs. The EW vacuum, where the relation $\sqrt{\phi_1^2 + \phi_2^2} = 246$ GeV is satisfied, is located on the pink line. One can see that the dark-green points have a tendency to be along the axes, and the most of VEVs after the last step PTs are located in the direction of the EW vacuum. In the left panel of Fig. 5, the VEVs after the first step PTs extend to in the directions of the ϕ_1 or ϕ_2 axis, even though many of them extend to the ϕ_2 axis. We find that those cases have the negative

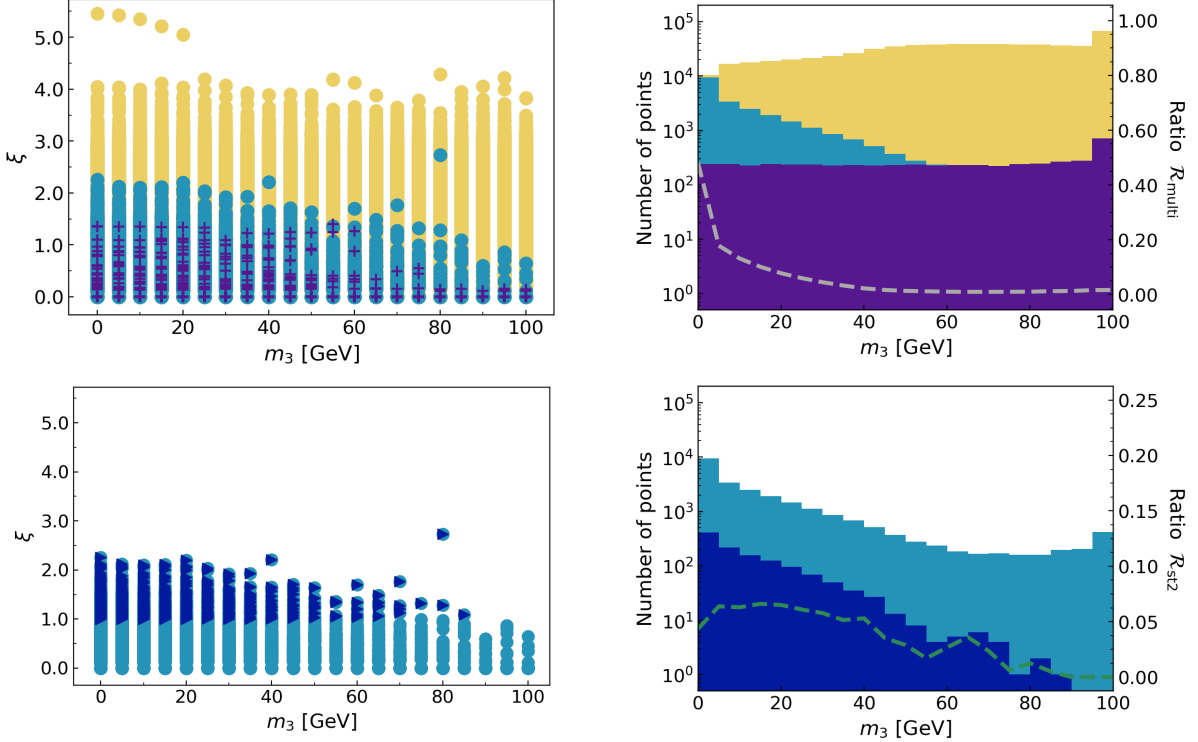


FIG. 6. Left: Parameter points where the 1-step and multi-step PTs (upper), and the strong 2-step PTs (lower) occur in the ξ vs. m_3 plane in the Type-I 2HDM with $m_A = m_{H^\pm}$. Right: Number of points where the 1-step and multi-step PTs (upper), and the strong 2-step PTs (lower) occur as a function of m_3 . The grey (upper) and green (lower) dashed lines represent $\mathcal{R}_{\text{multi}}$ and \mathcal{R}_{st2} , respectively. The way to color is the same as in Fig. 2.

m_1^2 or m_2^2 with the large magnitude as expected. Additionally, it is found that the VEVs after the first step PTs are located on or near the ϕ_1 axis when $\tan\beta \simeq 2$, $\cos(\beta - \alpha)$ is large and m_3 is near zero. On the other hand, for the 3-step PTs in the right panel of Fig. 5, the VEVs after the first step PTs favor going along the ϕ_2 axis rather than ϕ_1 . The magnitudes of those VEVs after the first step PTs are not so large, therefore it would be difficult for the first step PT of the 3-step PTs to become the strongly first order. Similar results to above are also seen in the Type-I 2HDM with $m_H = m_{H^\pm}$ and the Type-X 2HDM with m_A or $m_H = m_{H^\pm}$.

Finally, the left panels of Fig. 6 show the strength of PT ξ of the first step PT as a function of the m_3 ¹⁰. Considering the tree-level potential V_0 in Eq. (4), the large m_3^2 makes the potential decrease in the region far from the axes and the magnitude of the negative m_2^2 small (cf. Eq.(38)). These make the directions of the first step PT toward the region far from axes, so that it is difficult for the multi-step PTs whose first step PTs occur along the axes to happen. From the analysis, we have found that the maximum magnitude of the VEVs after the first step of the multi-step PTs are gradually larger as m_3 gets smaller. Therefore, ξ of the first step PT has a tendency to be large for the smaller m_3 . We have also found that the larger $\mathcal{R}_{\text{multi}}$ and \mathcal{R}_{st2} are obtained for the smaller m_3 as in the right panels of Fig. 6. Note that no parameter points where the strong 2-step PTs occur were found in $m_3 \gtrsim 90$ GeV. We summarize in Tabs. III and IV in Appendix. B, the values or ranges of input parameters where the ratios $\mathcal{R}_{\text{multi}}$ and \mathcal{R}_{st2} have the maximum values, respectively, for Type-I and -X 2HDMs.

¹⁰ In Ref. [15], ξ of the 1-step PT is computed with the Parwani method. Compared with our result ($\xi \lesssim 6$ as shown in the upper left panel of Fig. 6), the larger values of ξ such as $\xi \gtrsim 20$ have been obtained, however the explored parameter ranges in Ref. [15] is larger (e.g., $0 \leq m_3^2 \leq 5 \times 10^5$ GeV² and $1 \leq \tan\beta \leq 35$ in the Type-I 2HDM).

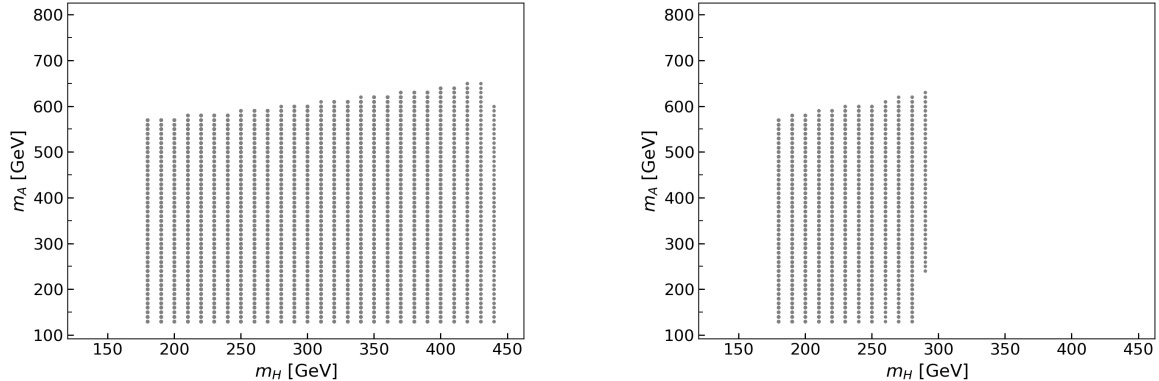


FIG. 7. Parameter regions in the m_A vs. m_H plane allowed by the theoretical constraints (the BFB, the perturbativity, and the tree-level unitarity) in the Type-I 2HDM with $m_H = m_{H\pm}$. The left and right panel show the regions in the cases of $\tan\beta = 2$ and 7, respectively. The other input parameters follow Tab. II.

2. Type-I ($m_H = m_{H\pm}$)

Fig. 7 represents the allowed parameter region by the theoretical constraints (the BFB, the perturbativity, and the tree-level unitarity) in the m_A vs. m_H plane at $\tan\beta = 2$ (left) and 7 (right) in the Type-I 2HDM with $m_H = m_{H\pm}$. We can see the theoretical constraints on m_H at $\tan\beta = 7$ is more severe than the ones at $\tan\beta = 2$, as $m_H \lesssim 290$ (440) GeV for $\tan\beta = 7$ (2).

Fig. 8 shows the parameter points where the 1-step, 2-step, and 3 or more step PTs (left), and the strong 2-step PTs (right) occur in the Type-I 2HDM with $m_H = m_{H\pm}$ for the m_A vs. m_H (first line), m_A vs. $\tan\beta$ (second line), m_A vs. $\cos(\beta - \alpha)$ (third line), and ξ vs. m_3 (fourth line) planes, respectively. Here the constraint from the stability of the EW vacuum is imposed. It is weaker than that in the Type-I 2HDM with $m_A = m_{H\pm}$, since the maximum mass scale of the extra scalar fields is lower due to the smaller maximal value of $m_{H\pm} (= m_H < 450$ GeV). The ranges of m_A where the multi-step PTs occur are larger as the $\tan\beta$ and $\cos(\beta - \alpha)$ decrease, respectively, in the left panels of the second and third lines in Fig. 8. Here the number of points where multi-step PTs occur in $\tan\beta \simeq 10$ and $\cos(\beta - \alpha) \simeq 0.25$ is respectively found to be small as in the Type-I with $m_A = m_{H\pm}$. On the other hand, we can see, from the upper three left panels of Fig. 8, there is a region that only the multi-step PTs occur in $m_A \gtrsim 600$ GeV and $m_H \gtrsim 410$ GeV with $\tan\beta \simeq 2$ and $\cos(\beta - \alpha) \simeq -0.25$. Such a region could be confirmed by the extra Higgs boson search for $A \rightarrow HZ$ at the LHC. In the bottom left panel of Fig. 8, the maximum value of ξ for the first step PT increases as m_3 gets smaller and reaches around 2. Moreover, we have found that the ratio $\mathcal{R}_{\text{multi}}$ has the maximum value when $m_A - m_H$ is negative with the large magnitude like -210 GeV as in the Type-I 2HDM with $m_A = m_{H\pm}$ (cf. Tab. III of Appendix B). Additionally, $\mathcal{R}_{\text{multi}}$ have maximum values at $\tan\beta \simeq 2$, $\cos(\beta - \alpha) \simeq -0.25$, and $m_3 \simeq 0$, respectively.

The strong 2-step PTs occur in $m_A \gtrsim 440$ GeV and $m_H \lesssim 360$ GeV with the mass hierarchy $m_A > m_H$ in the top right panel of Fig. 8. We can also see that they happen only in $\tan\beta \lesssim 4$ and $\cos(\beta - \alpha) \lesssim 0$ from the right panels of the second and third lines. In addition, the small m_3 is favored when the strong 2-step PTs happen in the bottom right panel. Some parameter points in the above region are excluded by the constraint from $B \rightarrow \mu^+\mu^-$, e.g. most of the points for the multi-step PTs with $m_H \simeq 330$ – 340 GeV. Besides, we have clarified that the ratio \mathcal{R}_{st2} is the largest in $m_A - m_H > 0$, the small $\tan\beta$, $\cos(\beta - \alpha)$, and m_3 , respectively, as shown in Tab. IV of Appendix B. These tendencies are not changed even if we consider the constraint from $B \rightarrow \mu^+\mu^-$.

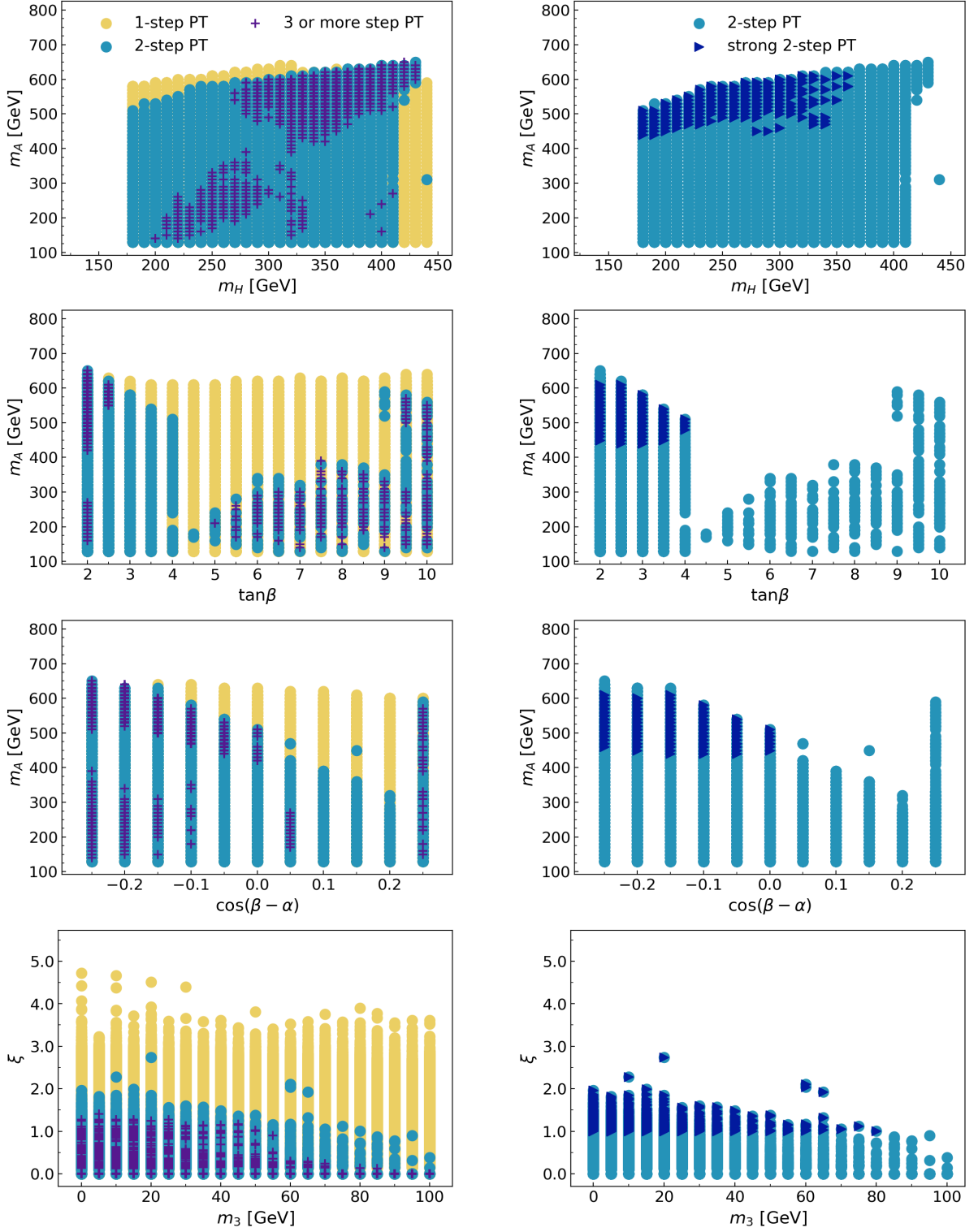


FIG. 8. Same as Figs. 2 and 6 but for the Type-I 2HDM with $m_H = m_{H^\pm}$.

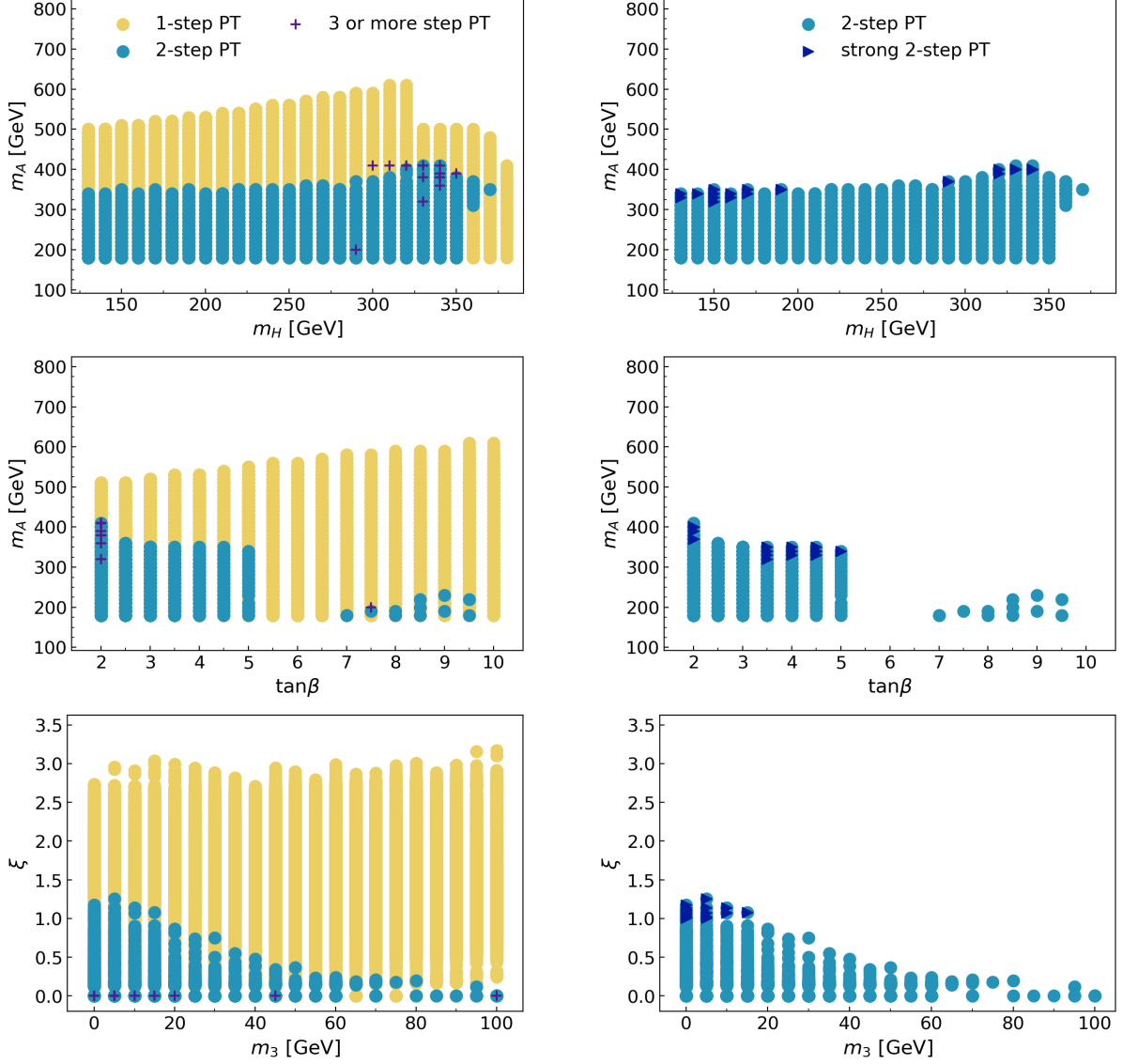


FIG. 9. Parameter points where the 1-step and multi-step PTs (left), and the strong 2-step PTs (right) occur in the m_A vs. m_H (top), m_A vs. $\tan\beta$ (middle), and ξ vs. m_3 (bottom) planes in the Type-X 2HDM with $m_A = m_{H^\pm}$. The way to color points is the same as in Fig. 2. Note that we set $\cos(\beta - \alpha) = 0$.

B. Type-X

1. Type-X ($m_A = m_{H^\pm}$)

In the cases of the Type-X 2HDMs, we take the alignment limit $\cos(\beta - \alpha) = 0$. Fig. 9 presents the parameter points where the 1-step and multi-step PTs (left), and the strong 2-step PTs (right) occur in the Type-X 2HDM with $m_A = m_{H^\pm}$, for the m_A vs. m_H (top), m_A vs. $\tan\beta$ (middle), and ξ vs. m_3 (bottom) planes.

In the top left panel of Fig. 9, the range of m_A where the multi-step PTs occur does not change much for $m_H \lesssim 350$ GeV. The middle left panel shows that most of the multi-step PTs occur in $\tan\beta \lesssim 5$. From the bottom left panel, we can see that the maximum value of ξ for the multi-step

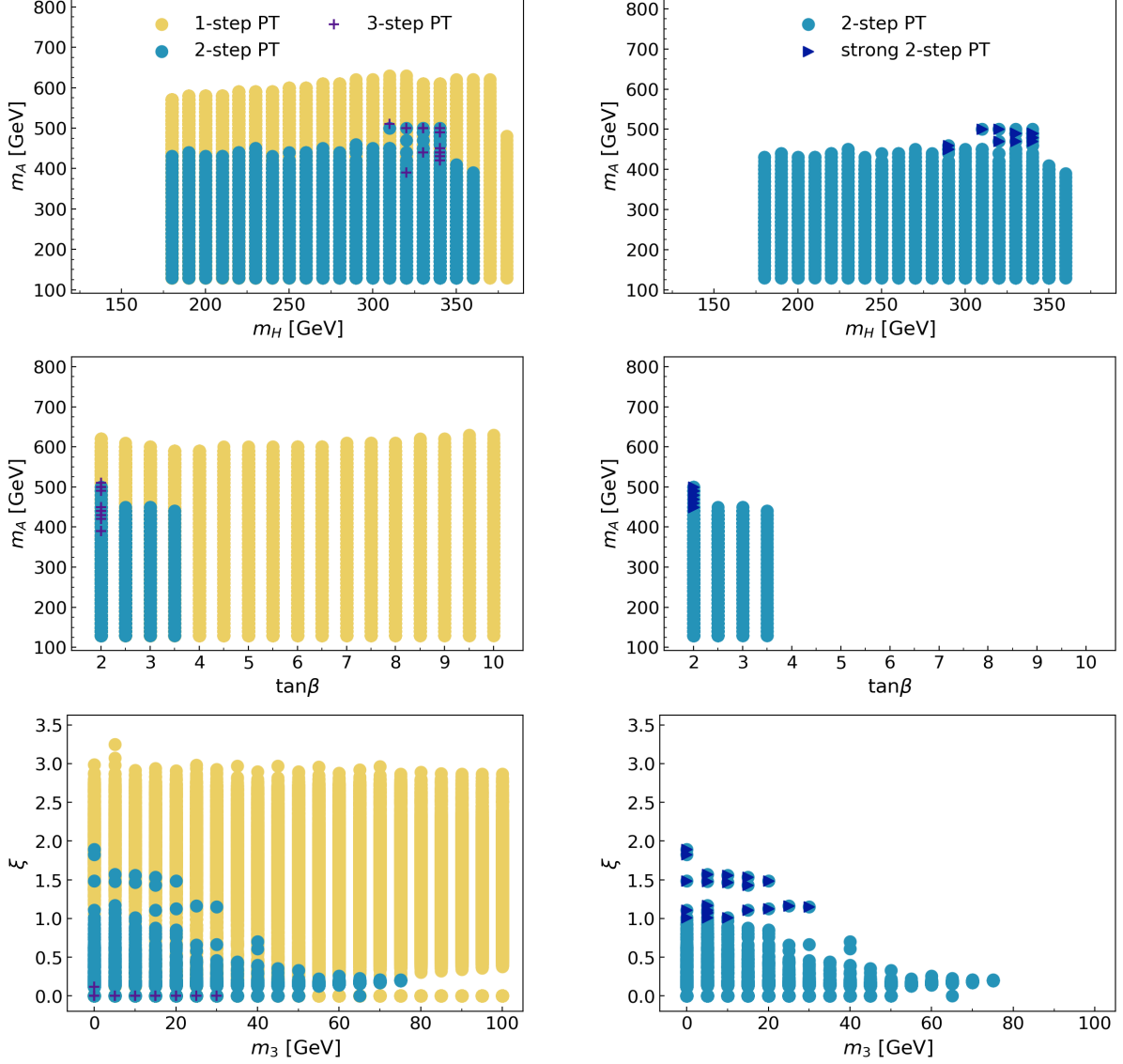


FIG. 10. Same as Fig. 9 but for the Type-X 2HDM with $m_H = m_{H^\pm}$.

PTs increases as m_3 decreases and reaches around 1.2. From our analyses, $\mathcal{R}_{\text{multi}}$ in the Type-X with $m_A = m_{H^\pm}$ has the largest value as 21% at $m_A - m_H \simeq -130$ GeV. It also gets the maximum value at $\tan\beta \simeq 2$ and $m_3 \simeq 0$, respectively. We have found that the region for the multi-step PTs with $m_A - m_H \simeq -130$ GeV is realized for $\tan\beta \simeq 2$ in this case, so that such a region is excluded by the constraints from both the $B \rightarrow \mu^+\mu^-$ and $H \rightarrow AZ$ [108]. In the allowed region by $B \rightarrow \mu^+\mu^-$ constraint, we have also found that the $\mathcal{R}_{\text{multi}}$ has the larger value for the $m_A - m_H < 0$, e.g. $\mathcal{R}_{\text{multi}} = 9\%$ for $m_A - m_H \simeq -90$ GeV, and the smaller $\tan\beta$, respectively.

On the other hand, the strong 2-step PTs only occur in the narrow region with $m_A > m_H$ as shown in the top right panel of Fig. 9. Moreover, the bottom right panel of Fig. 9 shows that the strong 2-step PTs happen only in $m_3 \lesssim 15$ GeV and they predict $\xi \simeq 1-1.3$. Although the points for the strong 2-step PTs do not receive the constraint from $B \rightarrow \mu^+\mu^-$, those with $m_H \simeq 150$ GeV would be excluded by the $A \rightarrow HZ$ search [108], while those with $m_H \simeq 330$ GeV remain.

As above, the parameter region where the multi-step PTs occur in this case gets narrow com-

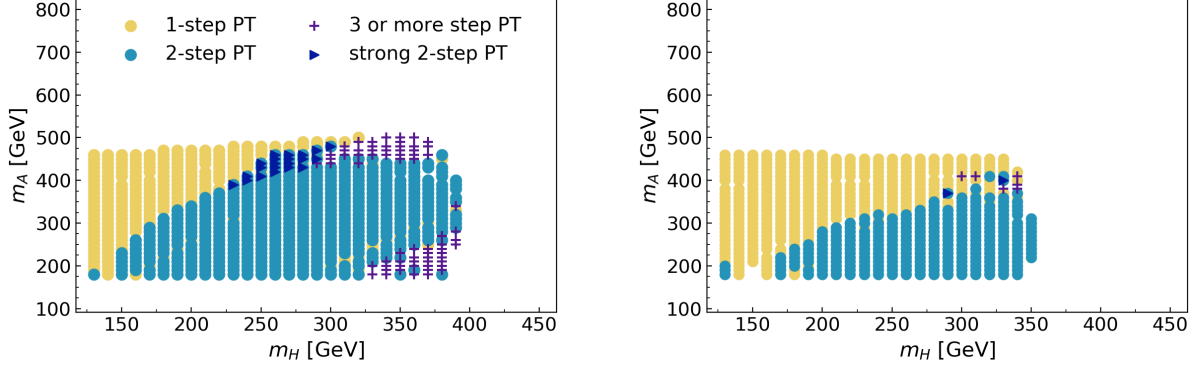


FIG. 11. Parameter points where the 1-step, 2-step, strong 2-step, and 3 or more step PTs occur in the m_A vs. m_H plane in the Type-I 2HDM with $m_A = m_{H^\pm}$. The left (right) panel shows the results at $\tan\beta = 2$, $\cos(\beta - \alpha) = -0.2$ (0), and $m_3 = 0$.

pared with that in the Type-I 2HDM with $m_A = m_{H^\pm}$. The Yukawa coupling of the top quark is same among the types as in Tab. I, therefore the contribution of the top quark, which gives the fermion's largest contribution to V_{CW} , is not dependent on the types. According to this, the reason for the narrow region in the analysis would be the difference of the range of $\cos(\beta - \alpha)$. As proof of that, we have confirmed that the result for $\cos(\beta - \alpha) = 0$ in the Type-I 2HDM with $m_A = m_{H^\pm}$ have the same tendency as in the Type-X 2HDM with $m_A = m_{H^\pm}$.

2. Type-X ($m_H = m_{H^\pm}$)

Fig. 10 exhibits the parameter points where the 1-step and multi-step PTs (left), and the strong 2-step PTs (right) occur in the Type-X 2HDM with $m_H = m_{H^\pm}$, for the m_A vs. m_H (top), m_A vs. $\tan\beta$ (middle), and ξ vs. m_3 (bottom) planes. In this case we have found that there are no parameter points where the more than 3-step PTs occur, therefore the purple points show the points for only the 3-step PTs. Although the largest value of m_A for the multi-step PTs is larger than that in the Type-X with $m_A = m_{H^\pm}$, the other tendencies in Fig. 10 are similar. The maximum value of ξ for the multi-step PTs reaches near 2 in the bottom left panel. We have found that $\mathcal{R}_{\text{multi}}$ is the largest at $m_A - m_H \simeq -210$ GeV, $\tan\beta \simeq 2$, and $m_3 \simeq 0$, respectively (cf. Tab. III of Appendix B). However, the region with the large magnitude of the negative $m_A - m_H$, which is found at $\tan\beta \simeq 2$, is excluded by the constraint from $H \rightarrow AZ$ decay [108]. On the other hand, in the region where the $H \rightarrow AZ$ channel does not open, we find that $\mathcal{R}_{\text{multi}}$ is obtained for $m_A < m_H$ as *e.g.* $\mathcal{R}_{\text{multi}} = 5\%$ for $m_A - m_H \simeq -80$ GeV.

Meanwhile, from the top right panel in Fig. 10, same as the other cases, the strong 2-step PTs only occur when the mass hierarchy $m_A > m_H$ exists with $\tan\beta \simeq 2$. Additionally, they happen when m_3 is small as $m_3 \lesssim 30$ GeV in the bottom right panel of Fig. 10. The constraint from $B \rightarrow \mu^+ \mu^-$ excludes the part of the region where the multi-step PTs happen, *e.g.* 290 GeV $\lesssim m_H \lesssim 340$ GeV, hence the region for the strong 2-step PTs is excluded.

We have confirmed that the result for $\cos(\beta - \alpha) = 0$ in the Type-I 2HDM with $m_H = m_{H^\pm}$ have same tendency with the ones in the Type-X 2HDM with $m_H = m_{H^\pm}$.

To summarize briefly, the region where the multi-step PTs is likely to occur is where $m_A - m_H$

is negative with large magnitude, $\tan\beta$ is small, $\cos(\beta - \alpha)$ is negative and small in the Type-I 2HDMs (it is fixed at zero in the Type-X 2HDMs), and m_3 is small, respectively. Different from the feature of the multi-step PTs, the strong multi-step PTs occur only when the mass hierarchy $m_A > m_H$ exists, while the tendencies for the other parameters are similar. Finally, we show the results of two specific cases. Fig. 11 shows the parameter points where the 1-step, 2-step, strong 2-step, and 3 or more step PTs occur in the m_A vs. m_H plane in the Type-I 2HDM with $m_A = m_{H^\pm}$. The other input parameters are fixed as $\tan\beta = 2$, $\cos(\beta - \alpha) = -0.2$ (left panel) or 0 (right panel), and $m_3 = 0$. We can see the regions for the 1-step and multi-step PTs are almost divided. In addition, $\mathcal{R}_{\text{multi}}$ in the left panel of Fig. 11 is larger than that in the right panel, which implies the multi-step PTs favor the negative values of $\cos(\beta - \alpha)$. We can also find that the strong 2-step PTs occur only with the mass hierarchy $m_A > m_H$. The above features are also seen in the Type-I 2HDM with $m_H = m_{H^\pm}$. Note that the right panel of Fig. 11 has similar tendencies with the result in the Type-X 2HDM with $m_A = m_{H^\pm}$ as described before. Taking into account the constraint from $B \rightarrow \mu\mu$ decays, the region of $m_A (= m_{H^\pm}) \lesssim 340$ GeV is excluded. In the survival parameter space in the left panel of Fig. 11, the multi-step PTs occur mostly for $m_H \gtrsim 300$ GeV. The region might be tested by the extra Higgs boson search of $A \rightarrow HZ$ if $m_A - m_H > m_Z$.

VI. PHYSICAL SIGNATURES

A. Higgs trilinear couplings

In this section, to research the possibility of the verification of the multi-step PT by collider experiments, we discuss the Higgs trilinear coupling λ_{hhh} . The coupling λ_{hhh} is derived by calculating the third derivative of the effective potential with respect to the SM-like Higgs fields at the EW vacuum as

$$\lambda_{hhh} = \left. \frac{\partial^3 V_{\text{eff}}^{T=0}(\phi_1, \phi_2)}{\partial h^3} \right|_{(\phi_1, \phi_2) = (v_1, v_2)}, \quad (39)$$

with $V_{\text{eff}}^{T=0} \equiv V_0 + V_{\text{CW}} + V_{\text{CT}}$. The trilinear coupling corrected by the leading 1-loop contribution of the top quarks in the SM is written by

$$\lambda_{hhh}^{\text{SM}} \simeq \frac{3m_h^2}{v} \left[1 - \frac{N_c}{3\pi^2} \frac{m_t^4}{v^2 m_h^2} \right], \quad (40)$$

where N_c is the color number of the top quarks. We determine the deviation of the Higgs trilinear coupling from that in the SM as

$$\delta\lambda_{hhh} \equiv \frac{\lambda_{hhh} - \lambda_{hhh}^{\text{SM}}}{\lambda_{hhh}^{\text{SM}}}. \quad (41)$$

When $\delta\lambda_{hhh}$ is equal to zero, the coupling has the same value as in the SM. In the following, we analyze $\delta\lambda_{hhh}$ by the Type-I and -X 2HDMs.

The current limits on the Higgs trilinear coupling from Higgs pair production are $-4.2 < \delta\lambda_{hhh} < 10.9$ (at 95% CL) from ATLAS [109]. At the future measurement, like the HL-LHC, the limit could reach an accuracy of about 50–60% with 3 ab⁻¹ data [75], while the ILC operating at 500 GeV has the possibility to measure $\delta\lambda_{hhh}$ with 27% of precision [76].

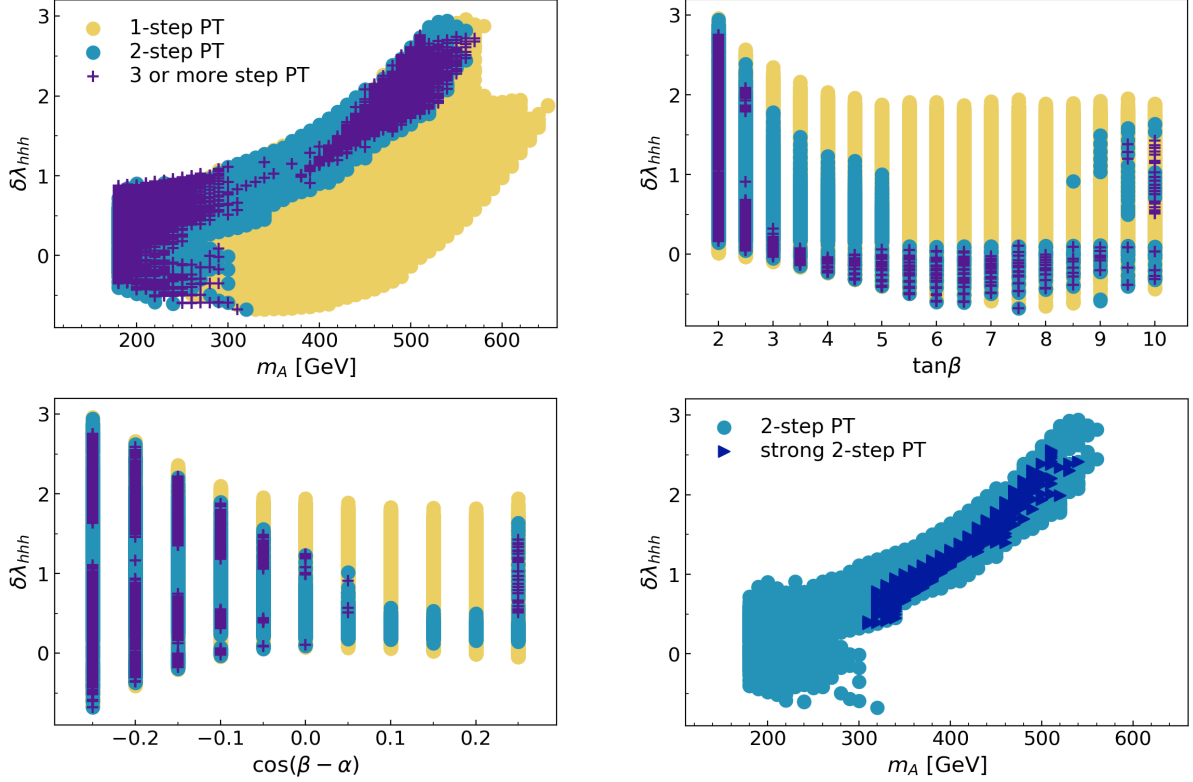


FIG. 12. Predictions for $\delta\lambda_{hhh}$ in the Type-I 2HDM with $m_A = m_{H^\pm}$. The panels except for the lower right panel show $\delta\lambda_{hhh}$ where the 1-step, 2-step, and 3 or more step PTs occur for m_A (upper left), $\tan\beta$ (upper right), and $\cos(\beta - \alpha)$ (lower left). The lower right plane shows $\delta\lambda_{hhh}$ where the 2-step and strong 2-step PTs happen for m_A .

1. Type-I ($m_A = m_{H^\pm}$)

Fig. 12 shows $\delta\lambda_{hhh}$ in the region where the 1-step, 2-step, and 3 or more step PTs occur in the Type-I 2HDM with $m_A = m_{H^\pm}$ as a function of m_A (upper left), $\tan\beta$ (upper right), and $\cos(\beta - \alpha)$ (lower left). In the upper left panel, the parameter points where the multi-step PTs happen are located on the upper side of the plots in the region $m_A \gtrsim 300$ GeV. In other words, compared with the results of the 1-step PTs, the values of $\delta\lambda_{hhh}$ for the multi-step PTs have a tendency to be large at the same value of m_A . The upper right panel shows the smaller $\tan\beta$ is, the larger the maximum value of $\delta\lambda_{hhh}$ is for $\tan\beta \lesssim 8$. In the lower left panel, when the multi-step PTs occur, the maximum value of $\delta\lambda_{hhh}$ becomes larger as $\cos(\beta - \alpha)$ gets smaller except for $\cos(\beta - \alpha) \simeq 0.25$, especially in the negative values of $\cos(\beta - \alpha)$. Note that there are parameter points that have the negative deviations. They are in $|\cos(\beta - \alpha)| \gtrsim 0.1$ and $m_3 \gtrsim 50$ GeV found out by our analysis. The region where $\delta\lambda_{hhh} \simeq 2.5$ for the multi-step PTs is $490 \text{ GeV} \lesssim m_A \lesssim 560 \text{ GeV}$, $\tan\beta \simeq 2$, and $\cos(\beta - \alpha) \lesssim -0.2$ in our parameter space. In the region, we find that m_H is in $320 \text{ GeV} \lesssim m_H \lesssim 410 \text{ GeV}$.

The lower right panel of Fig. 12 represents $\delta\lambda_{hhh}$ for the 2-step and strong 2-step PTs as a function of m_A . It indicates $\delta\lambda_{hhh}$ have the possibility of being large as 0.5–2.5 when the strong 2-step PTs happen. When $\delta\lambda_{hhh}$ is 2.5 with the strong 2-step PTs, we have found $m_A \simeq 510$ GeV, $m_H \simeq 320$ GeV, $\tan\beta \simeq 2$, and $\cos(\beta - \alpha) \simeq -0.25$. The deviations $\delta\lambda_{hhh} \simeq 0.5$ –2.5 would be tested at future colliders such as the HL-LHC and the ILC.

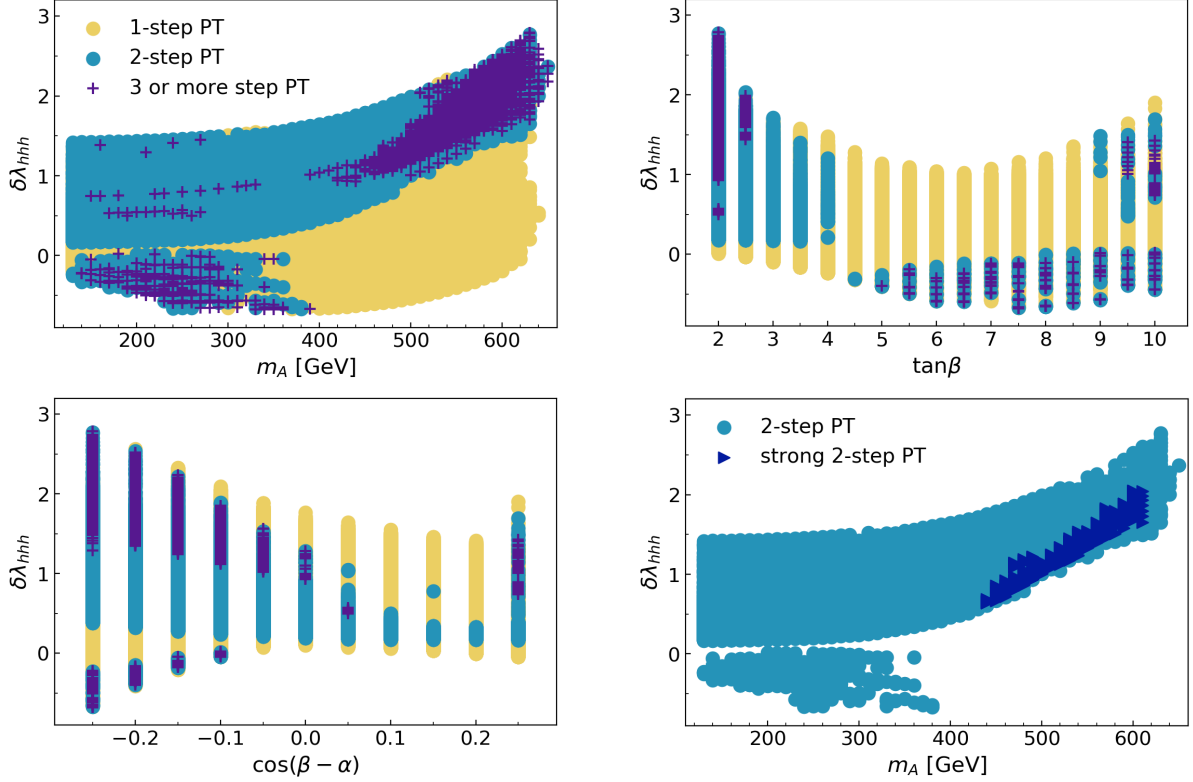


FIG. 13. Same as Fig. 12 but for the Type-I 2HDM with $m_H = m_{H^\pm}$.

2. Type-I ($m_H = m_{H^\pm}$)

The deviations $\delta\lambda_{hhh}$ for the Type-I 2HDM with $m_H = m_{H^\pm}$ are shown in Fig. 13. In the upper left panel, the parameter points where the multi-step PTs occur are located on the upper side in $m_A \gtrsim 400$ GeV. The behavior of the predictions for the multi-step PTs in Fig. 13 are similar to the ones in the Type-I 2HDM with $m_A = m_{H^\pm}$. From panels except for the lower right panel in Fig. 13, we find that the region where the multi-step PTs occur with $\delta\lambda_{hhh} \simeq 2.5$ is $590 \text{ GeV} \lesssim m_A \lesssim 640 \text{ GeV}$, $\tan\beta \simeq 2$, and $\cos(\beta - \alpha) \lesssim -0.2$. In the region, the range of m_H is $370 \text{ GeV} \lesssim m_H \lesssim 420 \text{ GeV}$. Additionally, in the lower right panel of Fig. 13, the range of $\delta\lambda_{hhh}$ for the strong 2-step PTs occur is about 0.5–2.0, while the largest value of such $\delta\lambda_{hhh}$ is slightly smaller than that in the Type-I 2HDM with $m_A = m_{H^\pm}$. When $\delta\lambda_{hhh}$ is 2 with the strong 2-step PTs, we have found $600 \text{ GeV} \lesssim m_A \lesssim 610 \text{ GeV}$, $300 \text{ GeV} \lesssim m_H \lesssim 360 \text{ GeV}$, $\tan\beta \simeq 2$, and $\cos(\beta - \alpha) \lesssim -0.15$. Although the constraint from $B \rightarrow \mu^+ \mu^-$ excludes the part of the above region (especially the region with $m_H \simeq 330\text{--}340$ GeV as described in Section V A 2), it still remains and such $\delta\lambda_{hhh}$ would be tested at the future collider experiments.

3. Type-X ($m_A = m_{H^\pm}$)

Fig. 14 gives $\delta\lambda_{hhh}$ in the region where the 1-step, 2-step, and 3 or more step PTs occur in the Type-X 2HDM with $m_A = m_{H^\pm}$ as a function of m_A (upper left), $\tan\beta$ (upper right), and m_3 (lower left). We take $\cos(\beta - \alpha) = 0$ (alignment limit) in the Type-X 2HDMs. In the upper left panel, the shape of the region where the multi-step PTs occur is narrow, hence the value of $\delta\lambda_{hhh}$ is predictable when m_A is fixed. The largest value of $\delta\lambda_{hhh}$ for the multi-step PTs is about 1.2

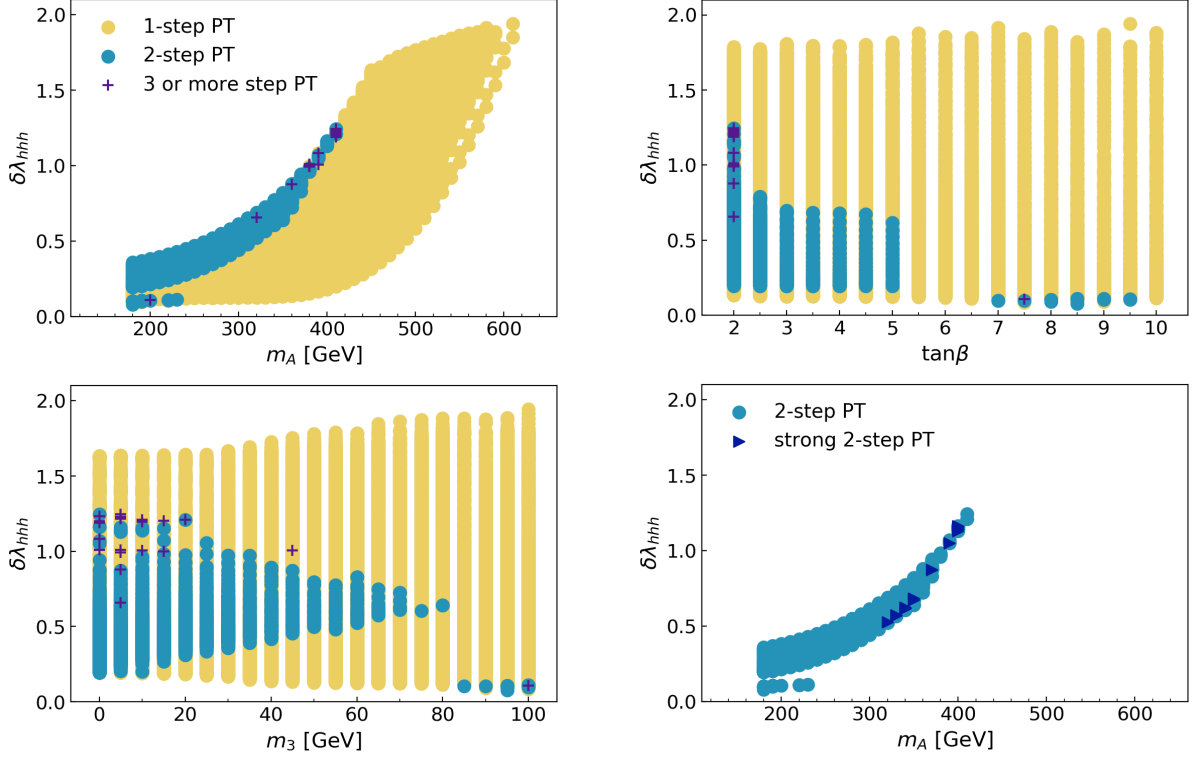


FIG. 14. Predictions for $\delta\lambda_{hhh}$ in the Type-I 2HDM with $m_A = m_{H^\pm}$. The panels except for the lower right panel show $\delta\lambda_{hhh}$ where the 1-step, 2-step, and 3 or more step PTs occur for m_A (upper left), $\tan\beta$ (upper right), and m_3 (lower left). The lower right plane shows $\delta\lambda_{hhh}$ where the 2-step and strong 2-step PTs happen for m_A .

at $m_A \simeq 400$ GeV, $\tan\beta \simeq 2$, and $m_3 \lesssim 20$ GeV, and 310 GeV $\lesssim m_H \lesssim 340$ GeV. Although the largest value is smaller than that in the Type-I 2HDMs, it can be accessed at the future collider experiments. The lower left panel shows that the values of $\delta\lambda_{hhh}$ for the multi-step PTs converge to around 0.7 as m_3 gets larger. Such dependence of $\delta\lambda_{hhh}$ on m_3 is not seen in the Type-I 2HDMs. Moreover, the predicted values of $\delta\lambda_{hhh}$ stay positive in all regions, although the negative $\delta\lambda_{hhh}$ are also predicted in the Type-I 2HDMs. These differences between the Type-I and Type-X are mainly due to the range of $\cos(\beta - \alpha)$. The lower right panel in Fig. 14 shows that the range where the strong 2-step PTs occur is $0.5 \lesssim \delta\lambda_{hhh} \lesssim 1.2$. When $\delta\lambda_{hhh}$ is 1.2 with the strong 2-step PTs, we have found $m_A \simeq 400$ GeV, $m_H \simeq 340$ GeV, and $\tan\beta \simeq 2$. The deviations $\delta\lambda_{hhh} \simeq 0.5\text{--}1.2$ would be explored at the future colliders like the HL-LHC and the ILC.

4. Type-X ($m_H = m_{H^\pm}$)

The deviations $\delta\lambda_{hhh}$ in the Type-X 2HDM with $m_H = m_{H^\pm}$ are shown in Fig. 15. We obtain similar features to the ones in the Type-X 2HDM with $m_A = m_{H^\pm}$, except that the region where the multi-step PTs occur gets broad upward. From Fig. 15 except for the lower right panel (also from the top left panel in Fig. 10), we see that $\delta\lambda_{hhh} \simeq 1.2$ for the multi-step PTs is predicted for 480 GeV $\lesssim m_A \lesssim 510$ GeV, $\tan\beta \simeq 2$, $m_3 \lesssim 30$ GeV, and 310 GeV $\lesssim m_H \lesssim 340$ GeV. However, this region is excluded by the constraint from $B \rightarrow \mu^+\mu^-$ as described in Section VB2. Nevertheless, when $m_A \simeq 400$ GeV, the maximum value of $\delta\lambda_{hhh} \simeq 0.9$ is allowed by the constraint, where the other parameters are $\tan\beta \simeq 2$, $m_3 \lesssim 40$ GeV, and $m_H \simeq 350$ GeV. Such a value of $\delta\lambda_{hhh}$ can

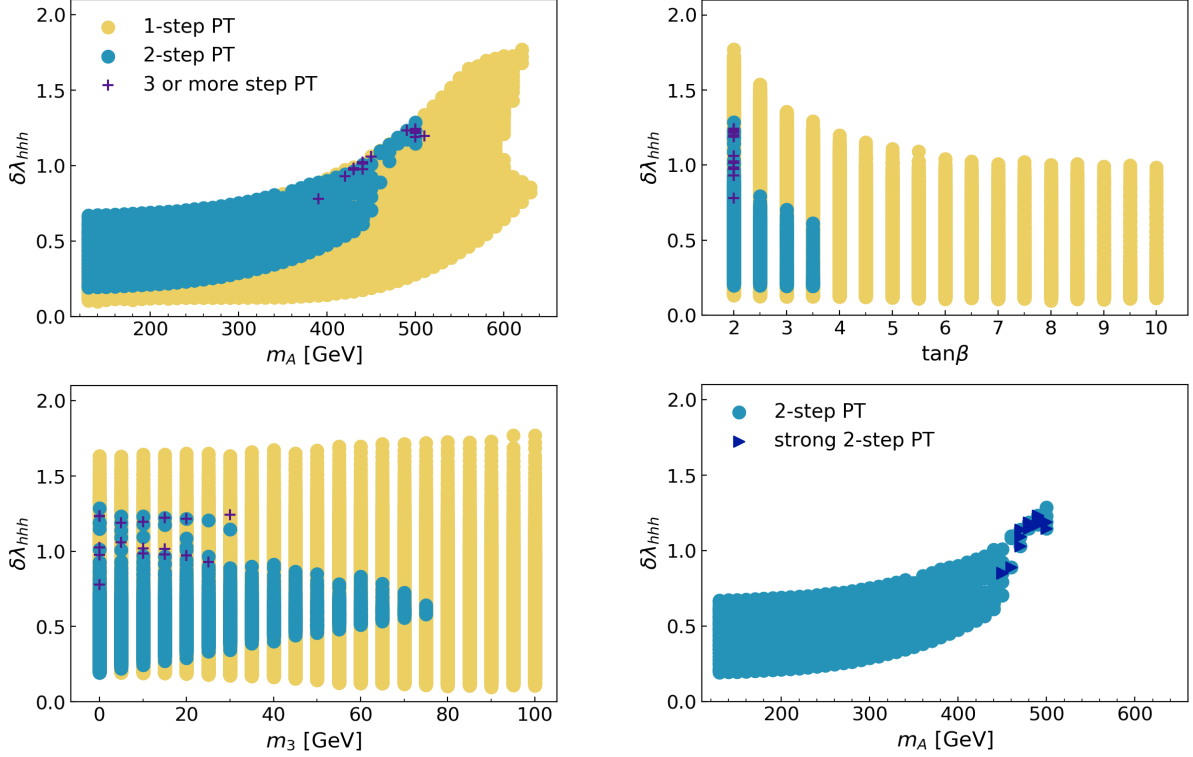


FIG. 15. Same as Fig. 14 but for the Type-X 2HDM with $m_H = m_{H^\pm}$.

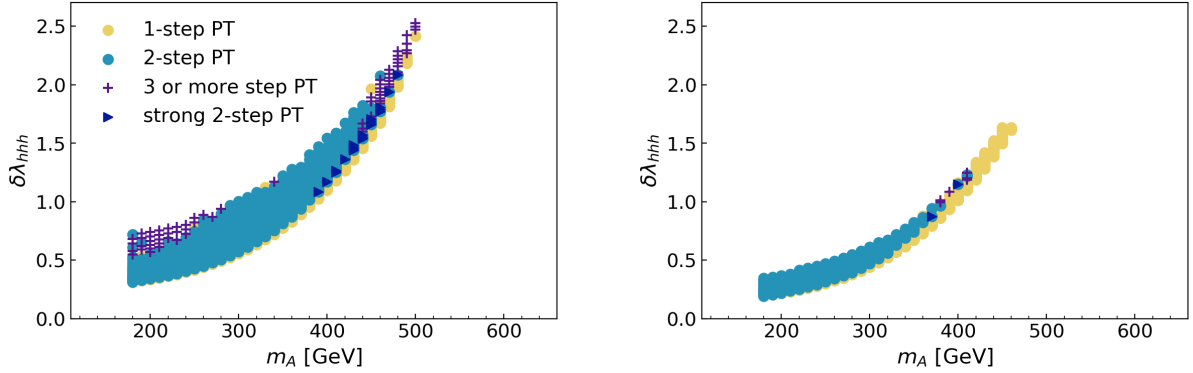


FIG. 16. Predictions for $\delta\lambda_{hhh}$ where the 1-step, 2-step, strong 2-step, and 3 or more step PTs occur for m_A in the Type-I 2HDM with $m_A = m_{H^\pm}$. The left (right) panel shows $\delta\lambda_{hhh}$ at $\tan\beta = 2$, $\cos(\beta - \alpha) = -0.2$ (0) and $m_3 = 0$.

be tested at the future collider experiments. In the lower right panel in Fig. 15, we see that the strong 2-step PTs give $\delta\lambda_{hhh} \simeq 1.2$ around $m_A \simeq 490$ GeV. However, all regions where the strong 2-step PTs occur is excluded by the constraint from $B \rightarrow \mu^+ \mu^-$ as mentioned in Section VB 2.

Fig. 16 shows the predictions for $\delta\lambda_{hhh}$ in the two cases in Fig. 11. In the left (right) panel of Fig. 16, we take $\tan\beta = 2$, $\cos(\beta - \alpha) = -0.2$ (0), and $m_3 = 0$ in the Type-I 2HDM with $m_A = m_{H^\pm}$. Compared with the same value of m_A , $\delta\lambda_{hhh}$ for the multi-step PTs have a tendency to be larger than that for the 1-step PTs. We can also see the largest value of $\delta\lambda_{hhh}$ where the multi-step PTs occur at $\cos(\beta - \alpha) = -0.2$ (left) is greater than that at $\cos(\beta - \alpha) = 0$ (right).

Meanwhile, $\delta\lambda_{hhh}$ for the strong 2-step PTs are relatively large as about $\delta\lambda_{hhh} \simeq 1\text{--}2$ (left) and $\simeq 1$ (right), respectively. The regions of the strong 2-step PTs do not receive the constraint from $B \rightarrow \mu\mu$ decays since $m_A(= m_{H^\pm}) > 340$ GeV.

B. Gravitational waves from multi-step PT

The first order PT at the EW scale is the source of GW whose typical spectrum has a peak frequency. Therefore if the first order PT occurs multiple times in a multi-step EWPT, the multi-peaked GW can be observed in the space-based interferometers. In this subsection, we study such a possibility in the case of the 2-step PT.

The GW spectrum is characterized by two parameters α_{GW} and $\tilde{\beta}_{\text{GW}}$ at the nuclear temperature T_n . Here T_n is determined by the condition that one bubble nucleates per Hubble radius $S_3/T_n \simeq 140$ where S_3 is the O(3) symmetric action. The α_{GW} is given by

$$\alpha_{\text{GW}} \equiv \frac{\epsilon(T_n)}{\rho_{\text{rad}}(T_n)}, \quad (42)$$

which is the ratio of the latent heat $\epsilon(T_n)$ to the radiation density $\rho_{\text{rad}}(T_n) = g_*(\pi^2 T_n^4)/30$ where g_* is 110.75 in the 2HDMs. The latent heat in the first order PT is calculated as

$$\epsilon(T_n) = \left[-\Delta V + T \frac{\partial \Delta V}{\partial T} \right] \Big|_{T=T_n}, \quad (43)$$

where ΔV is the difference between the effective potential of two phases before and after the PT. On the other hand, $\tilde{\beta}_{\text{GW}}$ is defined as $\tilde{\beta}_{\text{GW}} \equiv \beta_{\text{GW}}/H_n$, where H_n is the Hubble parameter at T_n and β_{GW} is the inverse time duration of the PT

$$\beta_{\text{GW}} \equiv H_n T_n \frac{d}{dT} \left(\frac{S_3(T)}{T} \right) \Big|_{T=T_n}. \quad (44)$$

There are three contributions to the GW spectrum at a first order PT:

$$h^2 \Omega_{\text{GW}}(f) = h^2 \Omega_\varphi(f) + h^2 \Omega_{\text{sw}}(f) + h^2 \Omega_{\text{turb}}(f). \quad (45)$$

Here h is the dimensionless Hubble parameter, f is the frequency of the GW at present, Ω_φ is the scalar field contribution from collisions of bubble walls [110–115], Ω_{sw} is the contribution from sound waves surrounding the bubble walls [116–119] and Ω_{turb} is the contribution from magnetohydrodynamic (MHD) turbulence in plasma [120–125]. Each contribution is given by α_{GW} and $\tilde{\beta}_{\text{GW}}$ with the velocity of bubble wall v_w and the κ_φ , κ_{sw} , and κ_{turb} which are the fraction of vacuum energy, respectively, converted into gradient energy of scalar field, bulk motion of the fluid, and MHD turbulence. Numerical simulations and analytic estimates of the individual contributions lead to the following formula:

- Scalar field contribution Ω_φ [115] :

$$h^2 \Omega_\varphi(f) = 1.67 \times 10^{-5} \tilde{\beta}_{\text{GW}}^{-2} \left(\frac{\kappa_\varphi \alpha_{\text{GW}}}{1 + \alpha_{\text{GW}}} \right)^2 \left(\frac{100}{g_*} \right)^{1/3} \left(\frac{0.11 v_w^3}{0.42 + v_w^2} \right) \frac{3.8 (f/f_\varphi)^{2.8}}{1 + 2.8 (f/f_\varphi)^{3.8}}, \quad (46)$$

where the peak frequency is

$$f_\varphi = 16.5 \times 10^{-6} \tilde{\beta}_{\text{GW}} \left(\frac{0.62}{1.8 - 0.1 v_w + v_w^2} \right) \left(\frac{T_n}{100 \text{ GeV}} \right) \left(\frac{g_*}{100} \right)^{1/6} \text{ Hz}. \quad (47)$$

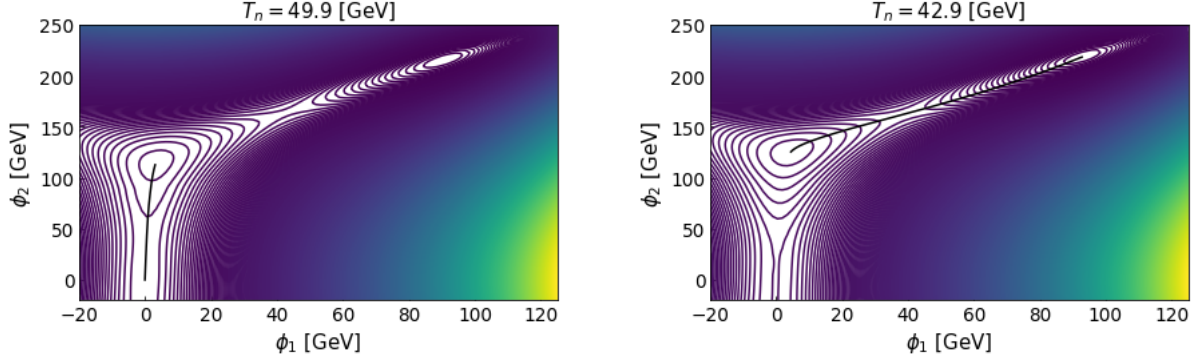


FIG. 17. Left (Right) : Contour plots of the effective potential and the path of the first (second) step PT at $T_n = 49.9$ (42.9) GeV for the benchmark point.

- Sound-wave contribution Ω_{sw} [119] :

$$h^2 \Omega_{\text{sw}}(f) = 2.65 \times 10^{-6} \tilde{\beta}_{\text{GW}}^{-1} \left(\frac{\kappa_{\text{sw}} \alpha_{\text{GW}}}{1 + \alpha_{\text{GW}}} \right)^2 \left(\frac{100}{g_*} \right)^{1/3} v_w (f/f_{\text{sw}})^3 \left(\frac{7}{4 + 3(f/f_{\text{sw}})^2} \right)^{7/2}, \quad (48)$$

where the peak frequency is

$$f_{\text{sw}} = 1.9 \times 10^{-5} v_w^{-1} \tilde{\beta}_{\text{GW}} \left(\frac{T_n}{100 \text{ GeV}} \right) \left(\frac{g_*}{100} \right)^{1/6} \text{ Hz}. \quad (49)$$

- MHD turbulence contribution Ω_{turb} [124, 125] :

$$h^2 \Omega_{\text{turb}}(f) = 3.35 \times 10^{-4} \tilde{\beta}_{\text{GW}}^{-1} \left(\frac{\kappa_{\text{turb}} \alpha_{\text{GW}}}{1 + \alpha_{\text{GW}}} \right)^{3/2} \left(\frac{100}{g_*} \right)^{1/3} v_w \frac{(f/f_{\text{turb}})^3}{[1 + (f/f_{\text{turb}})]^{11/3} (1 + 8\pi f/h_n)} \quad (50)$$

where the peak frequency is

$$f_{\text{turb}} = 2.7 \times 10^{-5} v_w^{-1} \tilde{\beta}_{\text{GW}} \left(\frac{T_n}{100 \text{ GeV}} \right) \left(\frac{g_*}{100} \right)^{1/6} \text{ Hz}, \quad (51)$$

and

$$h_n = 1.65 \times 10^{-5} \left(\frac{T_n}{100 \text{ GeV}} \right) \left(\frac{g_*}{100} \right)^{1/6} \text{ Hz}. \quad (52)$$

We assume the bubble wall velocity as $v_w = 1$ for simplicity and set [113, 126]

$$\kappa_\varphi \simeq \frac{1}{1 + 0.715 \alpha_{\text{GW}}} \left(0.715 \alpha_{\text{GW}} + \frac{4}{27} \sqrt{\frac{3 \alpha_{\text{GW}}}{2}} \right), \quad (53)$$

$$\kappa_{\text{sw}} \simeq \frac{\alpha}{0.73 + 0.083 \sqrt{\alpha_{\text{GW}}} + \alpha_{\text{GW}}}, \quad (54)$$

and $\kappa_{\text{turb}} \approx 0.1 \kappa_{\text{sw}}$ [119].

We compute the GW spectrums from a strong 2-step PT where both the first and second step PTs are first order. The following parameter set in the Type-I 2HDM is chosen as a benchmark point :

$$m_A = m_{H^\pm} = 490 \text{ GeV}, \quad m_H = 300 \text{ GeV}, \quad \tan \beta = 2.3, \quad \cos(\beta - \alpha) = -0.21, \quad m_3 = 20 \text{ GeV}.$$

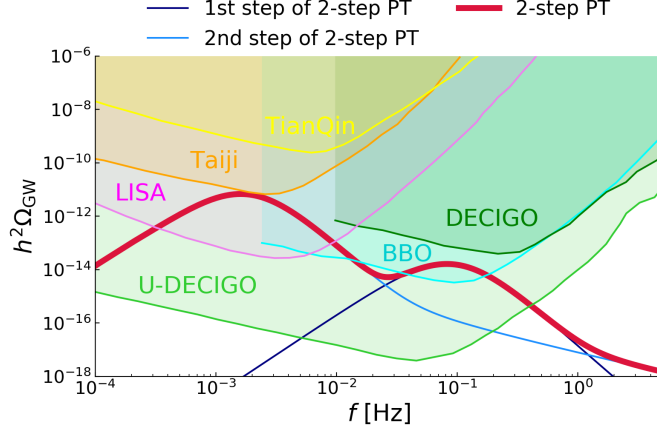


FIG. 18. GW spectrums from the first and second step of the strong 2-step PT for the benchmark point. The navy and blue lines represent the GW spectrums from the first and second step PTs, respectively. The red line shows the superposed GW spectrum.

In the left and right panels in Fig. 17, the paths of the first and second PT in the strong 2-step PT are respectively shown by the black line in the ϕ_2 vs. ϕ_1 plane. The contour plots of the effective potential at T_n are also given in Fig. 17. The path of the first step PT runs almost along the ϕ_2 axis from the origin to $(\phi_1, \phi_2) \simeq (3 \text{ GeV}, 115 \text{ GeV})$ at $T_n \simeq 49.9 \text{ GeV}$. The path of the second step PT goes from $(\phi_1, \phi_2) \simeq (5 \text{ GeV}, 126 \text{ GeV})$ to $(\phi_1, \phi_2) \simeq (93 \text{ GeV}, 219 \text{ GeV})$, which is in the direction of the EW vacuum, at $T_n = 42.9 \text{ GeV}$. The strengths of the first and second step PT are respectively $\xi = 2.1$ and 4.2, then both of them satisfy the criterion $\xi \geq 1$. The values of $(\alpha_{\text{GW}}, \tilde{\beta}_{\text{GW}})$ are $(8.1 \times 10^{-2}, 8.5 \times 10^3)$ for the first step and $(0.16, 1.9 \times 10^2)$ for the second step. The GW spectrums $h^2 \Omega_{\text{GW}}$ from these PTs are shown in Fig. 18. The observable areas by the future space-based interferometers such as LISA [30–32], DECIGO [127, 128], BBO [77], U-DECIGO [78], Taiji [129, 130], and TianQin [131, 132] are also presented. The navy and blue lines represent the GW spectrums from the first and second step PTs which have the peak frequencies around 0.1 Hz and 2×10^{-3} Hz, respectively. The superposed GW spectrum is shown by the red line. We can see that it has a double peak, which can be observed by BBO or U-DECIGO¹¹. Additionally, the deviation of the Higgs trilinear coupling $\delta\lambda_{hhh}$ is 2.2 for the benchmark point. Such $\delta\lambda_{hhh}$ has the possibility to be measured at the HL-LHC and the ILC. Therefore, the signature of the strong 2-step PT at the benchmark point may be observed in the experiments of both GW and colliders. With a combination of these signatures, it might be possible to identify whether the strong 2-step PT occurred in the early universe.

VII. CONCLUSIONS

In this paper, we have studied the parameter regions where the multi-step and strong 2-step EWPTs occur by scanning the parameter spaces in the CP-conserving Type-I and Type-X 2HDMs with m_A or $m_H = m_{H^\pm}$. In the analyses, we have focused on the small m_3 as $0 \leq m_3 \leq 100 \text{ GeV}$. As a result of our scan, areas where the multi-step and strong 2-step PTs occur have been found. The features of the parameter region where the multi-step PTs likely to occur are: (i) $m_A - m_H$

¹¹ Recent studies in Ref. [133] suggest the existence of an additional suppression factor for the Ω_{sw} due to the finite lifetime of the sound waves. The factors are about 0.005 and 0.1, respectively, for the first and second step PTs at our benchmark point. Taking into account the suppressions, the peak of the GW spectrum of the first step PT can be hardly seen. However, there are still several uncertainties in the calculation of the GW spectrum (see Refs. [134–143] for recent works).

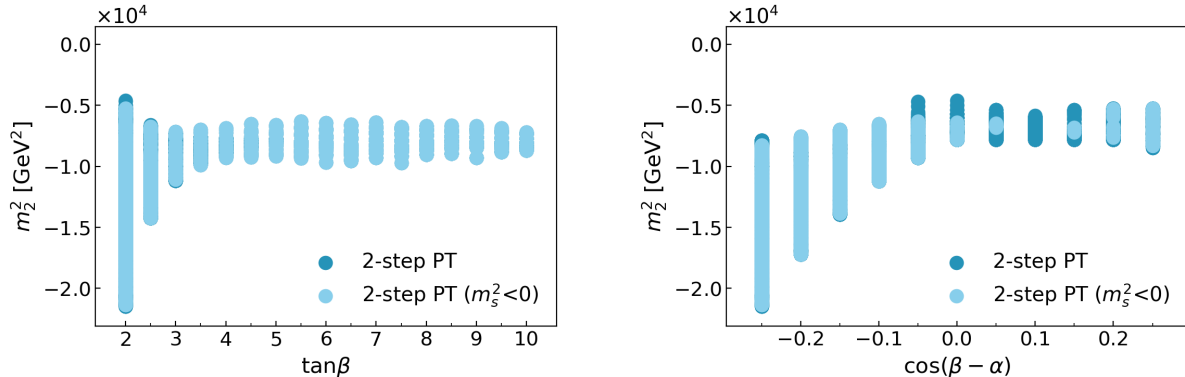


FIG. 19. Parameter points where the 2-step PTs (blue) and those with $m_s^2 < 0$ at the origin for the first step PTs (light-blue) occur in the m_2^2 vs. $\tan\beta$ (left) and m_2^2 vs. $\cos(\beta - \alpha)$ (right) planes in the Type-I 2HDM with $m_A = m_{H^\pm}$.

is negative with large magnitude, (ii) $\tan\beta$ is small, (iii) $\cos(\beta - \alpha)$ is negative and small, (iv) m_3 is small. The features (ii), (iii), and (iv) are preferred for the negative m_2^2 with large magnitude, which can yield the minimum point along the ϕ_2 axis. By contrast, the strong 2-step PTs occur only when the mass hierarchy $m_A > m_H$ exists in our parameter search, while they have similar features as (ii), (iii), and (iv). On the other hand, the VEVs after the first step of the multi-step PTs have a tendency to be located along the ϕ_2 (or ϕ_1) axis, and the VEVs after the last step PTs likely to lie in the direction of the EW vacuum.

As the possible physical signatures for the multi-step PTs in the collider experiments, we have investigated the deviation of the Higgs trilinear coupling from that in the SM $\delta\lambda_{hhh}$. The maximum value of $\delta\lambda_{hhh}$ increases as $\tan\beta$ and $\cos(\beta - \alpha)$ (which is zero in the Type-X 2HDMS) becomes smaller respectively in the case where the multi-step PTs occur. Compared with the results of the 1-step PTs at the same value of m_A , the values of $\delta\lambda_{hhh}$ for the multi-step PTs have a tendency to be large. In particular, when the strong 2-step PTs happen, $\delta\lambda_{hhh}$ are larger than about 0.5 and the largest value of $\delta\lambda_{hhh}$ in the Type-I 2HDMS reach over 2. Such deviations would be measured at future colliders like the HL-LHC and the ILC. As the signatures observed by the space-based interferometers, we have computed the GW spectrums from the strong 2-step PT where the first order PT occurs twice. The superposed GW spectrum has the possibility to have a double peak and be observed by the future observers as BBO and U-DECIGO. The multi-step EWPT might be confirmed by combining the information obtained from the future collider and GW experiments.

Appendix A: Complex effective potential at finite temperature

In this appendix, we comment on the region where the complex effective potential appears at finite temperature. Fig. 19 shows parameter points where the 2-step PTs occur for the negative scalar squared-masses at the origin for the first step PTs colored by light-blue in the Type-I 2HDM with $m_A = m_{H^\pm}$. The scalar squared-mass m_s^2 indicates the smallest squared-mass among the scalar fields. The parameter points for the 2-step PTs (blue) are the same as in Fig. 4. The light-blue points almost overlap with the points for the 2-step PTs except for $\cos(\beta - \alpha) \simeq -0.05$ – -0.15 . Although the light-blue points are widespread in the parameter space, a ratio of the number of points for the negative squared-masses to that for all points where the 2-step PTs occur is about 15%. On the other hand, we also find that the parameter points for the 1-step PTs are also widespread, and the number ratio is about 25%. Ref. [144] shows that the resummation method

	m_A [GeV]	m_H [GeV]	$m_A - m_H$ [GeV]	$\tan \beta$	$\cos(\beta - \alpha)$	m_3 [GeV]
Type-I ($m_A = m_{H^\pm}$)	130–550 ($\sim 7\%$)	390 (47%)	–250 (100%)	2 (11%)	–0.25 (9%)	0 (48%)
Type-I ($m_H = m_{H^\pm}$)	650 (100%)	360 (35%)	–210 (21%)	2 (13%)	–0.25 (9%)	0 (60%)
Type-X ($m_A = m_{H^\pm}$)	310 (11%)	350 (36%)	–130 (21%)	2 (13%)	-	0 (49%)
Type-X ($m_H = m_{H^\pm}$)	130–350 ($\sim 14\%$)	350 (38%)	–210 (50%)	2 (18%)	-	0 (60%)

TABLE III. Values or ranges of input parameters where $\mathcal{R}_{\text{multi}}$ have the maximum values. The values inside the parentheses represent the maximum values of $\mathcal{R}_{\text{multi}}$.

	m_A [GeV]	m_H [GeV]	$m_A - m_H$ [GeV]	$\tan \beta$	$\cos(\beta - \alpha)$	m_3 [GeV]
Type-I ($m_A = m_{H^\pm}$)	470 (41%)	280 (12%)	210 (100%)	2.5–4.5 ($\sim 10\%$)	–0.25 (11%)	20 (7%)
Type-I ($m_H = m_{H^\pm}$)	580 (50%)	280 (8%)	310 (100%)	2.5–4 ($\sim 11\%$)	–0.25 (9%)	10 (5%)

TABLE IV. Values of input parameters where $\mathcal{R}_{\text{st}2}$ have the maximum values. The values inside the parentheses represent the maximum values of $\mathcal{R}_{\text{st}2}$. Note that we omit the results for the Type-X 2HDMs because the number of points for the strong 2-step PTs in these cases are not large enough to consider the dependencies of the ratios on the input parameters.

	m_A [GeV]	m_H [GeV]	$m_A - m_H$ [GeV]	$\tan \beta$	$\cos(\beta - \alpha)$	m_3 [GeV]
Type-I ($m_A = m_{H^\pm}$)	400 (78%)	130 (39%)	220 (80%)	2 (34%)	0.05–0.25 ($\sim 36\%$)	0 (57%)
Type-I ($m_H = m_{H^\pm}$)	530 (83%)	130–340 (33%)	340 (91%)	2 (35%)	0.05–0.25 ($\sim 38\%$)	0 (66%)
Type-X ($m_A = m_{H^\pm}$)	400 (91%)	130 (39%)	210 (83%)	2 (40%)	-	0 (59%)
Type-X ($m_H = m_{H^\pm}$)	630 (100%)	360 (43%)	300 (85%)	2 (41%)	-	0 (64%)

TABLE V. Values or ranges of input parameters where $\mathcal{R}_{\text{st}1}$ have the maximum values. The values inside the parentheses represent the maximum values of $\mathcal{R}_{\text{st}1}$.

can cure the contributions from the negative squared-masses.

Appendix B: Tables for number analyses

We show in Tabs. III, and IV, the values or ranges of input parameters where the ratios $\mathcal{R}_{\text{multi}}$ (36), and $\mathcal{R}_{\text{st}2}$ (37) have the maximum values, respectively, for Type-I and -X 2HDMs. Note that we omit the results for the Type-X 2HDMs in Tab. IV because the number of points for the strong 2-step PTs in these cases are not large enough to consider the dependencies of the ratios on the input parameters. We see that *e.g.*, in Tab. III the multi-step PTs favor $m_A < m_H$ in all four cases. Similar tendencies in Tabs. III, and IV are seen even if we consider the constraint from $B \rightarrow \mu^+ \mu^-$.

Although we do not discuss the strong 1-step PTs in Section V, we also show the results of the number analyses for them because they are still important in the context of baryogenesis. Fig. 20 gives the number of points for the 1-step (yellow) and strong 1-step (orange) PTs, as a function of m_A (top), m_H (middle) and $m_A - m_H$ (bottom) in the Type-I 2HDM with $m_A = m_{H^\pm}$. The red dashed lines represent $\mathcal{R}_{\text{st}1}$, which are the ratios of the number of points for the strong 1-step PTs to that for the 1-step PTs,

$$\mathcal{R}_{\text{st}1} = \frac{\# \text{ of points for the strong 1-step PTs}}{\# \text{ of points for the 1-step PTs}}. \quad (\text{B1})$$

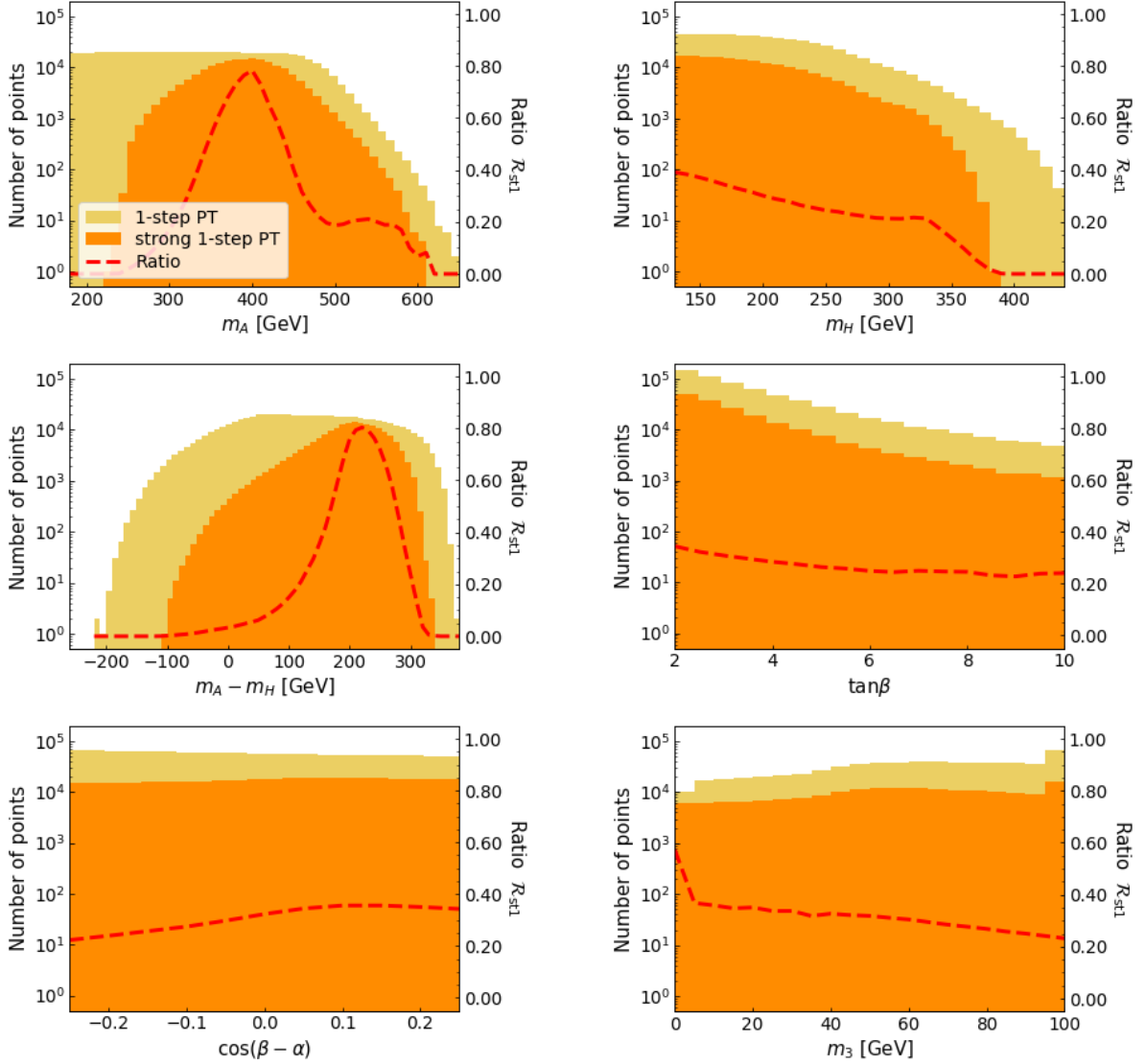


FIG. 20. Number of points where the 1-step (yellow) and strong 1-step (orange) PTs occur as a function of m_A , m_H , $m_A - m_H$, $\tan\beta$, $\cos(\beta - \alpha)$, and m_3 in the Type-I 2HDM with $m_A = m_{H^\pm}$. The red dashed line represents R_{st1} , which are the ratios of the number of points where the strong 1-step PTs occur to that for the 1-step PTs.

We see in the middle left panel that \mathcal{R}_{st1} peaks at $m_A - m_H \simeq 220$ GeV and reaches close to 1. Hence, the strong 1-step PTs favor the mass hierarchy $m_A > m_H$ (This is consistent with the results in Ref. [14]). This is the same feature as the one which the strong 2-step PTs have, shown in the top right panel of Fig. 3.

We show in Tab. V, the values or ranges of input parameters where the ratios \mathcal{R}_{st1} (B1) have the maximum values, respectively, for Type-I and -X 2HDMs. Similar tendencies in Tabs. III, IV, and V are seen even if we consider the constraint from $B \rightarrow \mu^+ \mu^-$.

ACKNOWLEDGMENTS

The work of M. A. is supported in part by the Japan Society for the Promotion of Sciences Grant-in-Aid for Scientific Research (Grant No. 17K05412 and No. 20H00160).

-
- [1] Planck Collaboration, N. Aghanim *et. al.*, *Astron. Astrophys.* **641** (2020) A6 [[1807.06209](#)].
 - [2] A. Sakharov *Sov. Phys. Usp.* **34** (1991), no. 5 392–393.
 - [3] V. Kuzmin, V. Rubakov and M. Shaposhnikov, *Phys. Lett. B* **155** (1985) 36.
 - [4] K. Kajantie, M. Laine, K. Rummukainen and M. E. Shaposhnikov, *Nucl. Phys. B* **466** (1996) 189–258 [[hep-lat/9510020](#)].
 - [5] F. Csikor, Z. Fodor and J. Heitger, *Phys. Rev. Lett.* **82** (1999) 21–24 [[hep-ph/9809291](#)].
 - [6] ATLAS Collaboration, G. Aad *et. al.*, *Phys. Lett. B* **716** (2012) 1–29 [[1207.7214](#)].
 - [7] ATLAS Collaboration Tech. Rep. ATLAS-CONF-2012-162, CERN, Geneva, Nov, 2012.
 - [8] CMS Collaboration, S. Chatrchyan *et. al.*, *Phys. Lett. B* **716** (2012) 30–61 [[1207.7235](#)].
 - [9] CMS Collaboration Tech. Rep. CMS-PAS-HIG-12-045, CERN, Geneva, 2012.
 - [10] M. D’Onofrio, K. Rummukainen and A. Tranberg, *Phys. Rev. Lett.* **113** (2014), no. 14 141602 [[1404.3565](#)].
 - [11] M. B. Gavela, P. Hernandez, J. Orloff and O. Pene, *Mod. Phys. Lett. A* **9** (1994) 795–810 [[hep-ph/9312215](#)].
 - [12] P. Huet and E. Sather, *Phys. Rev. D* **51** (1995) 379–394 [[hep-ph/9404302](#)].
 - [13] M. B. Gavela, P. Hernandez, J. Orloff, O. Pene and C. Quimbay, *Nucl. Phys. B* **430** (1994) 382–426 [[hep-ph/9406289](#)].
 - [14] G. Dorsch, S. Huber and J. No, *JHEP* **10** (2013) 029 [[1305.6610](#)].
 - [15] P. Basler, M. Krause, M. Muhlleitner, J. Wittbrodt and A. Wlotzka, *JHEP* **02** (2017) 121 [[1612.04086](#)].
 - [16] J. Bernon, L. Bian and Y. Jiang, *JHEP* **05** (2018) 151 [[1712.08430](#)].
 - [17] L. Wang, J. M. Yang, M. Zhang and Y. Zhang, *Phys. Lett. B* **788** (2019) 519–529 [[1809.05857](#)].
 - [18] W. Su, A. G. Williams and M. Zhang, *JHEP* **04** (2021) 219 [[2011.04540](#)].
 - [19] J. O. Andersen, T. Gorda, A. Helset, L. Niemi, T. V. I. Tenkanen, A. Tranberg, A. Vuorinen and D. J. Weir, *Phys. Rev. Lett.* **121** (2018), no. 19 191802 [[1711.09849](#)].
 - [20] K. Kainulainen, V. Keus, L. Niemi, K. Rummukainen, T. V. I. Tenkanen and V. Vaskonen, *JHEP* **06** (2019) 075 [[1904.01329](#)].
 - [21] A. Haarr, A. Kvellestad and T. C. Petersen, [1611.05757](#).
 - [22] G. C. Dorsch, S. J. Huber, T. Konstandin and J. M. No, *JCAP* **05** (2017) 052 [[1611.05874](#)].
 - [23] C.-Y. Chen, H.-L. Li and M. Ramsey-Musolf, *Phys. Rev. D* **97** (2018), no. 1 015020 [[1708.00435](#)].
 - [24] S. Kanemura, M. Kubota and K. Yagyu, *JHEP* **08** (2020) 026 [[2004.03943](#)].
 - [25] N. Blinov, J. Kozaczuk, D. E. Morrissey and C. Tamarit, *Phys. Rev. D* **92** (2015), no. 3 035012 [[1504.05195](#)].
 - [26] A. Hammerschmitt, J. Kripfganz and M. Schmidt, *Z. Phys. C* **64** (1994) 105–110 [[hep-ph/9404272](#)].
 - [27] L. Fromme, S. J. Huber and M. Seniuch, *JHEP* **11** (2006) 038 [[hep-ph/0605242](#)].
 - [28] E. Witten *Phys. Rev. D* **30** (1984) 272–285.
 - [29] C. Hogan *Mon. Not. Roy. Astron. Soc.* **218** (1986) 629–636.
 - [30] C. Caprini *et. al.*, *JCAP* **04** (2016) 001 [[1512.06239](#)].
 - [31] LISA Collaboration, P. Amaro-Seoane *et. al.*, [1702.00786](#).
 - [32] C. Caprini *et. al.*, *JCAP* **03** (2020) 024 [[1910.13125](#)].
 - [33] S. Profumo, M. J. Ramsey-Musolf and G. Shaughnessy, *JHEP* **08** (2007) 010 [[0705.2425](#)].
 - [34] J. R. Espinosa, T. Konstandin and F. Riva, *Nucl. Phys. B* **854** (2012) 592–630 [[1107.5441](#)].
 - [35] D. Curtin, P. Meade and C.-T. Yu, *JHEP* **11** (2014) 127 [[1409.0005](#)].
 - [36] M. Jiang, L. Bian, W. Huang and J. Shu, *Phys. Rev. D* **93** (2016), no. 6 065032 [[1502.07574](#)].
 - [37] F. P. Huang and C. S. Li, *Phys. Rev. D* **92** (2015), no. 7 075014 [[1507.08168](#)].
 - [38] G. Kurup and M. Perelstein, *Phys. Rev. D* **96** (2017), no. 1 015036 [[1704.03381](#)].
 - [39] Z. Kang, P. Ko and T. Matsui, *JHEP* **02** (2018) 115 [[1706.09721](#)].

- [40] T. Matsui *EPJ Web Conf.* **168** (2018) 05001 [[1709.05900](#)].
- [41] C.-W. Chiang, M. J. Ramsey-Musolf and E. Senaha, *Phys. Rev. D* **97** (2018), no. 1 015005 [[1707.09960](#)].
- [42] K. Hashino, M. Kakizaki, S. Kanemura, P. Ko and T. Matsui, *JHEP* **06** (2018) 088 [[1802.02947](#)].
- [43] F. P. Huang, Z. Qian and M. Zhang, *Phys. Rev. D* **98** (2018), no. 1 015014 [[1804.06813](#)].
- [44] C.-W. Chiang and B.-Q. Lu, *JHEP* **07** (2020) 082 [[1912.12634](#)].
- [45] M. Carena, Z. Liu and Y. Wang, *JHEP* **08** (2020) 107 [[1911.10206](#)].
- [46] P. Ghorbani [2010.15708](#).
- [47] L. Niemi, P. Schicho and T. V. I. Tenkanen, [2103.07467](#).
- [48] D. Land and E. D. Carlson, *Phys. Lett. B* **292** (1992) 107–112 [[hep-ph/9208227](#)].
- [49] A. Friedlander, I. Banta, J. M. Cline and D. Tucker-Smith, *Phys. Rev. D* **103** (2021), no. 5 055020 [[2009.14295](#)].
- [50] S. Fabian, F. Goertz and Y. Jiang, [2012.12847](#).
- [51] X. Wang, F. P. Huang and X. Zhang, *Phys. Rev. D* **101** (2020), no. 1 015015 [[1909.02978](#)].
- [52] H. H. Patel and M. J. Ramsey-Musolf, *Phys. Rev. D* **88** (2013) 035013 [[1212.5652](#)].
- [53] M. Chala, M. Ramos and M. Spannowsky, *Eur. Phys. J. C* **79** (2019), no. 2 156 [[1812.01901](#)].
- [54] N. F. Bell, M. J. Dolan, L. S. Friedrich, M. J. Ramsey-Musolf and R. R. Volkas, *JHEP* **05** (2020) 050 [[2001.05335](#)].
- [55] L. Niemi, M. Ramsey-Musolf, T. V. Tenkanen and D. J. Weir, [2005.11332](#).
- [56] H. H. Patel, M. J. Ramsey-Musolf and M. B. Wise, *Phys. Rev. D* **88** (2013), no. 1 015003 [[1303.1140](#)].
- [57] S. Inoue, G. Ovanesyan and M. J. Ramsey-Musolf, *Phys. Rev. D* **93** (2016) 015013 [[1508.05404](#)].
- [58] F. P. Huang and X. Zhang, *Phys. Lett. B* **788** (2019) 288–294 [[1701.04338](#)].
- [59] W. Chao, H.-K. Guo and J. Shu, *JCAP* **09** (2017) 009 [[1702.02698](#)].
- [60] M. J. Ramsey-Musolf, P. Winslow and G. White, *Phys. Rev. D* **97** (2018), no. 12 123509 [[1708.07511](#)].
- [61] T. Vieu, A. P. Morais and R. Pasechnik, *JCAP* **07** (2018) 014 [[1801.02670](#)].
- [62] A. P. Morais, R. Pasechnik and T. Vieu, [1802.10109](#).
- [63] L. Bian and X. Liu, *Phys. Rev. D* **99** (2019), no. 5 055003 [[1811.03279](#)].
- [64] R. Zhou, W. Cheng, X. Deng, L. Bian and Y. Wu, *JHEP* **01** (2019) 216 [[1812.06217](#)].
- [65] N. F. Bell, M. J. Dolan, L. S. Friedrich, M. J. Ramsey-Musolf and R. R. Volkas, *JHEP* **19** (2020) 012 [[1903.11255](#)].
- [66] A. P. Morais and R. Pasechnik, *JCAP* **04** (2020) 036 [[1910.00717](#)].
- [67] L. Bian, H.-K. Guo, Y. Wu and R. Zhou, *Phys. Rev. D* **101** (2020), no. 3 035011 [[1906.11664](#)].
- [68] S. Baum, M. Carena, N. R. Shah, C. E. M. Wagner and Y. Wang, [2009.10743](#).
- [69] T. Ghosh, H.-K. Guo, T. Han and H. Liu, [2012.09758](#).
- [70] T. Matsui, T. Nomura and K. Yagyu, [2102.09247](#).
- [71] S. Kanemura, S. Kiyoura, Y. Okada, E. Senaha and C. Yuan, *Phys. Lett. B* **558** (2003) 157–164 [[hep-ph/0211308](#)].
- [72] S. Kanemura, Y. Okada and E. Senaha, *Phys. Lett. B* **606** (2005) 361–366 [[hep-ph/0411354](#)].
- [73] J. Braathen and S. Kanemura, *Eur. Phys. J. C* **80** (2020), no. 3 227 [[1911.11507](#)].
- [74] F. Arco, S. Heinemeyer and M. J. Herrero, *Eur. Phys. J. C* **80** (2020), no. 9 884 [[2005.10576](#)].
- [75] M. Cepeda *et. al.*, *CERN Yellow Rep. Monogr.* **7** (2019) 221–584 [[1902.00134](#)].
- [76] K. Fujii *et. al.*, [1506.05992](#).
- [77] V. Corbin and N. J. Cornish, *Class. Quant. Grav.* **23** (2006) 2435–2446 [[gr-qc/0512039](#)].
- [78] H. Kudoh, A. Taruya, T. Hiramatsu and Y. Himemoto, *Phys. Rev. D* **73** (2006) 064006 [[gr-qc/0511145](#)].
- [79] V. D. Barger, J. L. Hewett and R. J. N. Phillips, *Phys. Rev. D* **41** (1990) 3421–3441.
- [80] Y. Grossman *Nucl. Phys. B* **426** (1994) 355–384 [[hep-ph/9401311](#)].
- [81] M. Aoki, S. Kanemura, K. Tsumura and K. Yagyu, *Phys. Rev. D* **80** (2009) 015017 [[0902.4665](#)].
- [82] M. Quiros pp. 187–259, 1, 1999. [hep-ph/9901312](#).
- [83] J. M. Cline, K. Kainulainen and M. Trott, *JHEP* **11** (2011) 089 [[1107.3559](#)].
- [84] L. Dolan and R. Jackiw, *Phys. Rev. D* **9** (1974) 3320–3341.
- [85] E. J. Weinberg and A. Wu, *Phys. Rev. D* **36** (1987) 2474–2480.
- [86] R. R. Parwani *Phys. Rev. D* **45** (1992) 4695 [[hep-ph/9204216](#)]. [Erratum: *Phys.Rev.D* 48, 5965

- (1993)].
- [87] P. B. Arnold and O. Espinosa, *Phys. Rev. D* **47** (1993) 3546 [[hep-ph/9212235](#)]. [Erratum: *Phys.Rev.D* 50, 6662 (1994)].
 - [88] M. Laine, M. Meyer and G. Nardini, *Nucl. Phys. B* **920** (2017) 565–600 [[1702.07479](#)].
 - [89] M. E. Carrington *Phys. Rev. D* **45** (1992) 2933–2944.
 - [90] N. Blinov, S. Profumo and T. Stefaniak, *JCAP* **07** (2015) 028 [[1504.05949](#)].
 - [91] N. G. Deshpande and E. Ma, *Phys. Rev. D* **18** (1978) 2574.
 - [92] M. Sher *Phys. Rept.* **179** (1989) 273–418.
 - [93] S. Nie and M. Sher, *Phys. Lett. B* **449** (1999) 89–92 [[hep-ph/9811234](#)].
 - [94] S. Kanemura, T. Kasai and Y. Okada, *Phys. Lett. B* **471** (1999) 182–190 [[hep-ph/9903289](#)].
 - [95] S. Kanemura, T. Kubota and E. Takasugi, *Phys. Lett. B* **313** (1993) 155–160 [[hep-ph/9303263](#)].
 - [96] A. G. Akeroyd, A. Arhrib and E.-M. Naimi, *Phys. Lett. B* **490** (2000) 119–124 [[hep-ph/0006035](#)].
 - [97] A. Barroso, P. Ferreira, I. Ivanov and R. Santos, *JHEP* **06** (2013) 045 [[1303.5098](#)].
 - [98] I. Ivanov and J. P. Silva, *Phys. Rev. D* **92** (2015), no. 5 055017 [[1507.05100](#)].
 - [99] C. L. Wainwright *Comput. Phys. Commun.* **183** (2012) 2006–2013 [[1109.4189](#)].
 - [100] H. E. Haber and D. O’Neil, *Phys. Rev. D* **83** (2011) 055017 [[1011.6188](#)].
 - [101] J. Haller, A. Hoecker, R. Kogler, K. Mönig, T. Peiffer and J. Stelzer, *Eur. Phys. J. C* **78** (2018), no. 8 675 [[1803.01853](#)].
 - [102] A. Arhrib, R. Benbrik, H. Harouiz, S. Moretti and A. Rouchad, [1810.09106](#).
 - [103] ATLAS Collaboration, G. Aad *et. al.*, *Phys. Rev. D* **101** (2020), no. 1 012002 [[1909.02845](#)].
 - [104] CMS Collaboration, V. Khachatryan *et. al.*, *Phys. Lett. B* **759** (2016) 369–394 [[1603.02991](#)].
 - [105] ATLAS Collaboration, M. Aaboud *et. al.*, *Phys. Lett. B* **783** (2018) 392–414 [[1804.01126](#)].
 - [106] CMS Collaboration, A. M. Sirunyan *et. al.*, *JHEP* **03** (2020) 055 [[1911.03781](#)].
 - [107] F. Kling, S. Su and W. Su, *JHEP* **06** (2020) 163 [[2004.04172](#)].
 - [108] S. Seidl, H. Day-Hall, S. Moretti and R. Benbrik, *Phys. Lett. B* **810** (2020) 135819 [[2006.05177](#)].
 - [109] ATLAS Collaboration Tech. Rep. ATLAS-CONF-2019-049, CERN, Geneva, Oct, 2019.
 - [110] A. Kosowsky, M. S. Turner and R. Watkins, *Phys. Rev. D* **45** (1992) 4514–4535.
 - [111] A. Kosowsky, M. S. Turner and R. Watkins, *Phys. Rev. Lett.* **69** (1992) 2026–2029.
 - [112] A. Kosowsky and M. S. Turner, *Phys. Rev. D* **47** (1993) 4372–4391 [[astro-ph/9211004](#)].
 - [113] M. Kamionkowski, A. Kosowsky and M. S. Turner, *Phys. Rev. D* **49** (1994) 2837–2851 [[astro-ph/9310044](#)].
 - [114] C. Caprini, R. Durrer and G. Servant, *Phys. Rev. D* **77** (2008) 124015 [[0711.2593](#)].
 - [115] S. J. Huber and T. Konstandin, *JCAP* **09** (2008) 022 [[0806.1828](#)].
 - [116] M. Hindmarsh, S. J. Huber, K. Rummukainen and D. J. Weir, *Phys. Rev. Lett.* **112** (2014) 041301 [[1304.2433](#)].
 - [117] J. T. Giblin, J and J. B. Mertens, *JHEP* **12** (2013) 042 [[1310.2948](#)].
 - [118] J. T. Giblin and J. B. Mertens, *Phys. Rev. D* **90** (2014), no. 2 023532 [[1405.4005](#)].
 - [119] M. Hindmarsh, S. J. Huber, K. Rummukainen and D. J. Weir, *Phys. Rev. D* **92** (2015), no. 12 123009 [[1504.03291](#)].
 - [120] C. Caprini and R. Durrer, *Phys. Rev. D* **74** (2006) 063521 [[astro-ph/0603476](#)].
 - [121] T. Kahniashvili, A. Kosowsky, G. Gogoberidze and Y. Maravin, *Phys. Rev. D* **78** (2008) 043003 [[0806.0293](#)].
 - [122] T. Kahniashvili, L. Campanelli, G. Gogoberidze, Y. Maravin and B. Ratra, *Phys. Rev. D* **78** (2008) 123006 [[0809.1899](#)]. [Erratum: *Phys.Rev.D* 79, 109901 (2009)].
 - [123] T. Kahniashvili, L. Kisslinger and T. Stevens, *Phys. Rev. D* **81** (2010) 023004 [[0905.0643](#)].
 - [124] C. Caprini, R. Durrer and G. Servant, *JCAP* **12** (2009) 024 [[0909.0622](#)].
 - [125] P. Binetruy, A. Bohe, C. Caprini and J.-F. Dufaux, *JCAP* **06** (2012) 027 [[1201.0983](#)].
 - [126] J. R. Espinosa, T. Konstandin, J. M. No and G. Servant, *JCAP* **06** (2010) 028 [[1004.4187](#)].
 - [127] N. Seto, S. Kawamura and T. Nakamura, *Phys. Rev. Lett.* **87** (2001) 221103 [[astro-ph/0108011](#)].
 - [128] S. Kawamura *et. al.*, *Class. Quant. Grav.* **28** (2011) 094011.
 - [129] W.-R. Hu and Y.-L. Wu, *Natl. Sci. Rev.* **4** (2017), no. 5 685–686.
 - [130] W.-H. Ruan, Z.-K. Guo, R.-G. Cai and Y.-Z. Zhang, *Int. J. Mod. Phys. A* **35** (2020), no. 17 2050075 [[1807.09495](#)].
 - [131] TianQin Collaboration, J. Luo *et. al.*, *Class. Quant. Grav.* **33** (2016), no. 3 035010 [[1512.02076](#)].
 - [132] X.-C. Hu, X.-H. Li, Y. Wang, W.-F. Feng, M.-Y. Zhou, Y.-M. Hu, S.-C. Hu, J.-W. Mei and C.-G.

- Shao, *Class. Quant. Grav.* **35** (2018), no. 9 095008 [[1803.03368](#)].
- [133] H.-K. Guo, K. Sinha, D. Vagie and G. White, *JCAP* **01** (2021) 001 [[2007.08537](#)].
- [134] D. Cutting, M. Hindmarsh and D. J. Weir, *Phys. Rev. Lett.* **125** (2020), no. 2 021302 [[1906.00480](#)].
- [135] X. Wang, F. P. Huang and X. Zhang, *JCAP* **05** (2020) 045 [[2003.08892](#)].
- [136] D. Croon, O. Gould, P. Schicho, T. V. I. Tenkanen and G. White, *JHEP* **04** (2021) 055 [[2009.10080](#)].
- [137] H.-K. Guo, K. Sinha, D. Vagie and G. White, [2103.06933](#).
- [138] O. Gould and T. V. I. Tenkanen, *JHEP* **06** (2021) 069 [[2104.04399](#)].
- [139] F. Giese, T. Konstandin and J. Van De Vis, *JCAP* **07** (2020), no. 07 057 [[2004.06995](#)].
- [140] S. Höche, J. Kozaczuk, A. J. Long, J. Turner and Y. Wang, *JCAP* **03** (2021) 009 [[2007.10343](#)].
- [141] F. Giese, T. Konstandin, K. Schmitz and J. Van De Vis, *JCAP* **01** (2021) 072 [[2010.09744](#)].
- [142] X. Wang, F. P. Huang and X. Zhang, *Phys. Rev. D* **103** (2021), no. 10 103520 [[2010.13770](#)].
- [143] X. Wang, F. P. Huang and X. Zhang, [2011.12903](#).
- [144] C. Delaunay, C. Grojean and J. D. Wells, *JHEP* **04** (2008) 029 [[0711.2511](#)].